Astrometry meets pulsar timing arrays: Synergies for gravitational wave detection

N. M. Jiménez Cruz,[1,*] Ameek Malhotra,[1,†] Gianmassimo Tasinato,[1,2,‡] and Ivonne Zavala[1,§]

[1]*Physics Department, Swansea University, Swansea SA28PP, United Kingdom*

[2]*Dipartimento di Fisica e Astronomia, Università di Bologna, INFN, Sezione di Bologna, I.S. FLAG, viale B. Pichat 6/2, 40127 Bologna, Italy*

(Received 10 January 2025; accepted 10 October 2025; published 30 October 2025)

High-precision astrometry offers a promising approach to detect low-frequency gravitational waves, complementing pulsar timing array (PTA) observations. We explore the response of astrometric measurements to a stochastic gravitational wave background (SGWB) in synergy with PTA data. Analytical, covariant expressions for this response are derived, accounting for the presence of a possible dipolar anisotropy in the SGWB. We identify the optimal estimator for extracting SGWB information from astrometric observations and examine how sensitivity to SGWB properties varies with the sky positions of stars and pulsars. Using representative examples of current PTA capabilities and near-future astrometric sensitivity, we demonstrate that cross-correlating astrometric and PTA data can improve constraints on SGWB properties, compared to PTA data alone. The improvement is quantified through Fisher forecasts for the SGWB amplitude, spectral tilt, and dipolar anisotropy amplitude. In the future, such joint constraints could play a crucial role in identifying the origin of SGWB signals detected by PTAs.

DOI: 10.1103/8k1p-pzcg

I. INTRODUCTION

The detection of a stochastic background of gravitational waves (SGWB) would represent a major milestone for gravitational wave astronomy. Recent exciting developments in the nano-Hertz (nHz) frequency regime suggest that we may be on the verge of a detection, with several pulsar timing array (PTA) collaborations reporting strong evidence for a SGWB in this range [1–10]. Hellings-Downs (HD) correlations [11], representing the "smoking-gun" signature of SGWB, have been detected with $2-4\sigma$ of statistical significance, depending on the dataset. Upcoming data from PTAs, in particular, the joint analysis from IPTA Data Release 3, are expected to further increase the significance of this detection and measure the SGWB amplitude and spectrum more precisely [9]. The observed signal may arise from mergers of supermassive black hole binaries (SMBHB) [12,13] or from early-universe sources [14] (or a combination of both), and the increasing precision offered by future data may help in identifying the origin of the SGWB. In the longer term, the Square Kilometre Array (SKA) [15,16], with its unparalleled timing precision and larger number of observed pulsars, will provide definitive measurements of the SGWB properties.

It is worthwhile to also explore alternative probes that could complement the PTA observations in the nHz regime. One such promising probe is astrometry—using the precise measurements of the positions of a very large number of distant sources to measure the effects of gravitational waves [17–35]. GWs present between the Earth and the source induce deflections in the observed positions of these sources (hereafter we lump all such sources under the umbrella term "stars"). Much like the pulsar timing residuals, which are correlated across different pulsars as a function of their angular separation, the astrometric deflections for different stars are also correlated, albeit with a slightly different form of the correlation as compared to the PTA HD correlation.

The success of the Gaia mission [36,37], which observes billions of stars with a precision measurement of their position of the order of the milli-arcsecond (mas), has spurred a renewed interest in astrometric detection of SGWB. Previously, data from very-long baseline interferometry (VLBI) [38] and, more recently, Gaia have already been used to set upper limits on the SGWB in the frequency range $10^{-18}\ \text{Hz} \lesssim f \lesssim 10^{-9}\ \text{Hz}$ [22,39–43]. The full Gaia data release 5 (DR5) with the individual time-series measurements will further extend this frequency range to

*Contact author: nmjc1209@gmail.com
†Contact author: ameek.malhotra@swansea.ac.uk
‡Contact author: g.tasinato2208@gmail.com
§Contact author: e.i.zavalacarrasco@swansea.ac.uk

$f \lesssim 4 \times 10^{-7}$ Hz (each star is observed roughly 14 times a year [36]). The upcoming Roman survey [44]—due to its much higher observing cadence—may even be able to push toward higher frequencies ($f \lesssim 10^{-4}$ Hz), opening up an additional observational window for GW [45–47]. Although current astrometric upper limits on the SGWB lie around the $\Omega_{\rm GW} \lesssim 10^{-2}$ level, the proposed mission Theia [48,49], with its μas astrometric precision, would represent a significant upgrade in terms of sensitivity to SGWB [32,42,50], even being competitive with PTA sensitivity.

Motivated by these considerations, in this work we investigate how data from astrometric surveys may be used to complement existing PTA experiments and potentially improve upon current SGWB measurements obtained from PTA data alone. We do this by means of a Fisher matrix analysis and calculate the improvement in constraints that can be achieved by cross-correlating timing residuals of PTAs with the angular deflections of astrometry, focusing on the parameters corresponding to the SGWB monopole amplitude, spectral tilt (for a power-law spectrum), and a possible dipole anisotropy magnitude. Along the way, we derive for the first time analytic covariant expressions for the response to dipole anisotropy in the SGWB, for astrometry as well as its cross-correlation with PTAs. The anisotropy of the nHz SGWB is a key observable that may be used to discriminate between astrophysical and cosmological origins of the SGWB given their differing predictions, with the magnitude of intrinsic cosmological SGWB anisotropies (see e.g., [51–59]) expected to be much smaller than their astrophysical counterpart [60–68]. Cosmological anisotropies of large magnitude include kinematic anisotropies due to motion with respect to the primordial source of SGWB [58,69–74]. For primordial sources of SGWB, we can expect a dipolar anisotropy with an amplitude 1000 times smaller than the isotropic part of the background, as found in cosmic microwave background (CMB) measurements [75–78]. Given that kinematic anisotropies of the SGWB are well motivated, we mainly consider a kinematic dipole as a specific target for our analysis, although it can be easily extended to discuss other anisotropies as well. Additional works discussing detection prospects of the anisotropies of the SGWB in different contexts are [60,61,79–85], with PTA specific analyses in [66,86–91]. See e.g., [92] for a review.

This paper is organized as follows: In Sec. II, we review the theory of SGWB detection with astrometry and the corresponding monopole response and overlap reduction functions. We then derive an analytic expression for the astrometric response to the kinematic dipole anisotropy and its autocorrelation. We also discuss the astrometry-redshift correlation for the SGWB monopole and derive an analytic expression for this cross-correlation in the presence of a dipole anisotropy. In Sec. III, we use these results to forecast the astrometric sensitivity to the SGWB monopole and dipole and also estimate the improvement in constraints that can be obtained by cross-correlating astrometry and PTA data, over PTA data alone. Finally, in Sec. IV, we present our conclusions. Two technical appendixes complement our discussion.

II. OVERLAP FUNCTIONS FOR ASTROMETRY AND PULSAR TIMING ARRAYS

The overlap reduction function (ORF) of a pair of detectors accounts for how the sensitivity to the SGWB changes due to the relative positions and orientations of the detectors. The cross-correlation of the signal across the two detectors can be written entirely in terms of the ORF and the underlying SGWB spectral density. Schematically, one can write

$$\langle s_I(f) s_J(f) \rangle \propto \gamma_{IJ}(f) I(f), \tag{2.1}$$

where $s_{I,J}$ denotes the signal at detector I, J, γ_{IJ} the overlap reduction function, and $I(f)$ the SGWB intensity. In this section, we obtain expressions for the astrometric ORFs and their cross-correlations with pulsar timing arrays. We include the possible presence of a dipolar SGWB anisotropy, which can be instrumental for distinguishing cosmological from astrophysical backgrounds. We investigate the crucial role of the position of the monitored objects for determining the sensitivity of the system to the SGWB properties. Our covariant, analytical formulas are convenient and simple to use for Fisher forecast analysis.

Astrometry aims to measure the position and motion of stars on the celestial sphere, while PTA are sensitive to the time of arrival of radio signals from distant pulsar sources. GW passing between the position of stars, pulsars, and the Earth modify photon geodesics, leading to effects which are measurable with both methods. The presence of a SGWB induces correlations among measurements of GW signals, as detected by observations of distinct astronomical objects. In most studies, the SGWB is assumed to be isotropic. However, it develops kinematic anisotropies if the frames of the GW source and GW detector move with respect to each other [69]. Kinematic anisotropies break the isotropy of the SGWB, making it direction dependent: They are fully determined by the properties of the isotropic part of the background, as well as the direction of the velocity among frames. For this reason, it is desirable to derive analytical, covariant expressions for the ORF, which make it transparent how the sensitivity to SGWB properties depends on the position of stars in the sky. We do so in Sec. II A, where we focus specifically on astrometry,

while in Sec. II B, we analyze its possible synergies with PTA observations.

A. Astrometry overlap functions

We define GW in terms of spin-2 fluctuations of the flat metric

$$ds^2 = -dt^2 + [\delta_{ij} + h_{ij}(t,\vec{x})]dx^i dx^j. \tag{2.2}$$

The transverse-traceless spin-2 tensors $h_{ij}(t,\vec{x})$ can be decomposed in Fourier modes as

$$h_{ij}(t,\vec{x}) = \sum_\lambda \int_{-\infty}^{+\infty} df \int d^2\mathbf{p}\, e^{-2\pi i f \mathbf{p}\cdot\vec{x}} e^{2\pi i f t} \mathbf{e}^\lambda_{ij}(\mathbf{p}) h_\lambda(f,\mathbf{p}), \tag{2.3}$$

where f is the GW frequency and $\mathbf{p}$ the unit vector indicating its direction, and $\mathbf{e}^\lambda_{ij}(\mathbf{p})$ are real polarization tensors in the basis $\lambda = (+,\times)$. Notice that we take the flat space limit of the GW evolution; hence, it satisfies a flat space d'Alembertian equation. We impose $h_\lambda(-f,\mathbf{p}) = h^*_\lambda(f,\mathbf{p})$. A GW passing between a star and the Earth causes a distortion δn^i on the star direction $\mathbf{n}$ at time t, given by the formula (see e.g., [25])

$$\delta n_i(t,\mathbf{n}) = \mathcal{R}_{ikl}(\mathbf{n},\mathbf{p}) h_{kl}(t,0), \tag{2.4}$$

where, as is customary, we focus on the so-called "Earth-term" contribution only (see e.g., [25,93]). We introduce

$$\mathcal{R}_{ikl}(\mathbf{n},\mathbf{p}) = \frac{n_k}{2}\left[\frac{(n_i+p_i)n_l}{1+\mathbf{n}\cdot\mathbf{p}} - \delta_{il}\right], \tag{2.5}$$

where recall that the unit vectors $\mathbf{n}$ and $\mathbf{p}$ indicate the direction of the star and of GW propagation, respectively. The three-index quantity $\mathcal{R}_{ikl}$ is orthogonal to the unit vector n_i when contracted with its first index.

In order to characterize the stochastic GW signal, we assume it has a Gaussian distribution with zero mean. Thus, the SGWB can be entirely characterized by its two-point function, expressed as

$$\langle h_{\lambda_1}(f_1,\mathbf{p}_1) h^*_{\lambda_2}(f_2,\mathbf{p}_2)\rangle = \frac{3H_0^2}{4\pi^2}\frac{\Omega_{\rm GW}(f_1,\mathbf{p}_1)}{f_1^3}\delta_{\lambda_1\lambda_2}\delta(f_1-f_2)\frac{\delta^{(2)}(\mathbf{p}_1-\mathbf{p}_2)}{4\pi}, \tag{2.6}$$

where the angle brackets denote an ensemble average, over all possible realizations of the SGWB, and $\Omega_{\rm GW}(f,\mathbf{p})$ is the quantity customarily used for characterizing the GW energy density per log frequency interval (see e.g., [94]). The spectral energy density parameter $\Omega_{\rm GW}$ is related to the GW intensity I through the relation

$$\Omega_{\rm GW}(f,\mathbf{p}) = \frac{4\pi^2 f^3}{3H_0^2} I(f,\mathbf{p}). \tag{2.7}$$

A SGWB can be characterized by anisotropies, which render $\Omega_{\rm GW}(f,\mathbf{p})$ explicitly dependent on the GW direction $\mathbf{p}$. We include here SGWB kinematic anisotropies [69], induced by the motion of the observer with respect to the GW background source. They can be a key observable for distinguishing astrophysical from cosmological backgrounds [58,69]. Denoting with $\beta = |\mathbf{v}|/c$ the size of the relative velocity among frames with respect to the speed of light, and $\mathbf{v}$ the velocity unit vector, we have [69]

$$\Omega_{\rm GW}(f,\mathbf{p}) = \bar{\Omega}_{\rm GW}(f) + \beta(4-n_\Omega)\mathbf{p}\cdot\mathbf{v}\bar{\Omega}_{\rm GW}(f), \tag{2.8}$$

where $\bar{\Omega}_{\rm GW}(f) = (4\pi)^{-1}\int d^2\mathbf{p}\Omega_{\rm GW}(f,\mathbf{p})$ is the angular averaged GW energy density. The result also depends on the energy density spectral tilt $n_\Omega \equiv d\ln\Omega_{\rm GW}/d\ln f$. The simple form of the SGWB anisotropy of Eq. (2.8) is all that we need to carry out our calculations. We include only the kinematic dipole contribution proportional to β, working under the hypothesis of small relative velocity among frames—supported by observations of the CMB dipolar anisotropy of the CMB temperature [75–78]. It is important to emphasize that kinematic effects are associated with deterministic—and not statistical—anisotropies. Hence, formula (2.8) fully characterizes the kinematic dipolar anisotropy, with no need for ensemble averaging. An implication is that our analysis of overlap functions can be conveniently carried out in a fully covariant way.

An alternative method would be to work in the spherical harmonic basis for the timing residuals and angular deflections; e.g., see [29,31,95–97]. For a full-sky survey with a uniform distribution of stars, spherical harmonics provide a convenient diagonal basis for analyzing the effects of the SGWB due to the orthogonality of the spherical harmonics. However, in general, the dataset used may not have a uniform distribution of sources or be full sky; e.g., see [42]. To keep our analysis completely general and applicable to arbitrary distributions of stars, we do not resort to the spherical harmonic decomposition.

We proceed by considering two-point correlators of star deflections as induced by GWs passing between stars and the Earth. Denoting with $\mathbf{n}$ and $\mathbf{q}$ the unperturbed directions of the two stars, respectively, we use Eqs. (2.4), (2.6), and (2.8) to find

$$\begin{aligned}\langle \delta n^i(\mathbf{n},t)\delta n^j(\mathbf{q},t')\rangle &= \frac{3H_0^2}{32\pi^3}\int df \frac{\bar{\Omega}_{\rm GW}(f)}{f^3} \\ &\quad\times \cos[2\pi f(t-t')][H^{(0)}_{ij}(\mathbf{n},\mathbf{q}) \\ &\quad + \beta(4-n_\Omega)H^{(1)}_{ij}(\mathbf{n},\mathbf{q},\mathbf{v})], \\ &= p_{(0)}H^{(0)}_{ij}(\mathbf{n},\mathbf{q}) + p_{(1)}H^{(1)}_{ij}(\mathbf{n},\mathbf{q},\mathbf{v}).\end{aligned} \tag{2.9}$$

The quantities $p_{(0,1)}$ depend on integrals along the frequency of the SGWB amplitude and its spectral tilt n_Ω. The tensors $H_{ij}^{(0)}$ and $H_{ij}^{(1)}$ are independent of frequency. They are formally expressed in terms of the following angular integrals:

$$H_{ij}^{(0)}(\mathbf{n},\mathbf{q}) = \int d^2\Omega_{\mathbf{p}}\, \mathcal{R}_{ikl}(\mathbf{n},\mathbf{p})\mathcal{R}_{jrs}(\mathbf{q},\mathbf{p})P_{klrs}, \tag{2.10}$$

$$H_{ij}^{(1)}(\mathbf{n},\mathbf{q},\mathbf{v}) = \int d^2\Omega_{\mathbf{p}}(\mathbf{p}\cdot\mathbf{v})\mathcal{R}_{ikl}(\mathbf{n},\mathbf{p})\mathcal{R}_{jrs}(\mathbf{q},\mathbf{p})P_{klrs}, \tag{2.11}$$

with the projector

$$\mathcal{R}_{ijk}(\mathbf{n},\mathbf{p}) = \frac{n_j}{2}\left[\frac{(n_i+p_i)n_k}{1+\mathbf{n}\cdot\mathbf{p}} - \delta_{ik}\right] \tag{2.12}$$

arising from properties of the polarization tensors in this context [25]. The tensors $H_{ij}^{(0,1)}$ are the analog of the PTA ORF relative to the monopolar and dipolar kinematic components of the SGWB. To compute these quantities, we introduce the projection tensor

$$\begin{aligned} P_{ijkl} = {} & \delta_{ik}\delta_{jl} + \delta_{il}\delta_{jk} - \delta_{ij}\delta_{kl} + p_i p_j p_k p_l \\ & - \delta_{ik}p_j p_l - \delta_{jl}p_i p_k - \delta_{il}p_j p_k - \delta_{jk}p_i p_l \\ & + \delta_{ij}p_k p_l + \delta_{kl}p_i p_j \end{aligned} \tag{2.13}$$

associated with combinations of polarization tensors $e_{ij}^{(\lambda)}$. The tensors $H_{ij}^{(0,1)}(\mathbf{n},\mathbf{q})$ are orthogonal to $\mathbf{n}$ in their first index and to $\mathbf{q}$ in their second index.

The integrals (2.10) and (2.11) can be performed with a standard method of contour integration used in the context of PTA physics; see e.g., [98].[1] For the case of the monopole, the ORF is associated with the integral in Eq. (2.10). We consider the combination

$$y = \frac{1-\mathbf{n}\cdot\mathbf{q}}{2} = \frac{1-\cos\zeta}{2} \tag{2.14}$$

controlling the angular separation between a pair of stars on the celestial sphere: This quantity lies in the interval $0 \le y \le 1$. The astrometry ORF relative to the monopolar, isotropic component of the SGWB is

$$\begin{aligned} H_{ij}^{(0)}(\mathbf{n},\mathbf{q}) = {} & \frac{\pi}{3(1-y)^2}(1-8y+7y^2-6y^2\ln y) \\ & \times[(2-2y)\delta_{ij} - n_i n_j - q_i q_j - q_i n_j \\ & + (1-2y)q_j n_i], \end{aligned} \tag{2.15}$$

a result equivalent to what was found in [25], although expressed slightly more compactly. As mentioned above, we obtained this expression by evaluating the integral (2.10) using contour integration. The expression (2.15) is the astrometry equivalent of the Hellings-Downs function, the PTA ORF for the SGWB monopole. From the statistical properties of the two-point correlators, one expects dependence only on the angular separation $\mathbf{n}\cdot\mathbf{q}$ between stars in (2.15). This feature is not immediately apparent in our results because of the tensorial structure introduced by the projection tensor (2.13), which brings explicit factors of n_i and q_j into the expression. A useful way to reveal this property is through the quantity $\mathrm{Tr}[\boldsymbol{H}_0\boldsymbol{H}_0]$,[2] which, as expected, depends only on the relative directions (see Appendix B). Alternative formulations that make the exclusive dependence on $\mathbf{n}\cdot\mathbf{q}$ manifest have also been explored; see e.g., [28,31].

The tensor defined by the integral (2.11) corresponds instead to the astrometry response function for dipolar kinematic anisotropies. It can be computed in terms of appropriate spherical harmonics [31]—but here we provide a covariant, succinct expression for it. We introduce, as in [25], a basis of vectors:

$$\mathbf{A} = \mathbf{n}\times\mathbf{q}, \qquad \mathbf{B} = \mathbf{n}\times\mathbf{A}, \qquad \mathbf{C} = -\mathbf{q}\times\mathbf{A}. \tag{2.16}$$

Computing the integral of Eq. (2.11) by means of contour integrations, we find

$$H_{ij}^{(1)} = a_1(A_iC_j + B_iA_j) + a_2(B_iC_j - A_iA_j), \tag{2.17}$$

with $a_{1,2}$ scalar coefficients depending on the angles among the vectors involved. Recalling the definition (2.14) and denoting

$$(Av) = \mathbf{v}\cdot(\mathbf{n}\times\mathbf{q}), \qquad (nv) = \mathbf{n}\cdot\mathbf{v}, \tag{2.18}$$

we express the coefficients $a_{1,2}$ as

$$a_1 = \frac{\pi(Av)(1-4y-\frac{3y^2\ln(y)}{1-y})}{6y(1-y)^2}, \tag{2.19}$$

[1] In fact, the calculation proceeds exactly as in [98]. We decompose the angular integration measure as $d^2\Omega_{\mathbf{p}} = d(\cos\theta)d\varphi$ and perform the substitution $\varphi = e^{iz}$. In this way, the resulting integral in the complex plane is expressed as a contour integral over $\mathcal{C}$, corresponding to the unit circle. The integrand has poles inside the unit circle, and the integral can be straightforwardly evaluated using Cauchy's integral formula and the residue theorem.

[2] This expression also plays an important role in the Fisher forecasts of Sec. III.

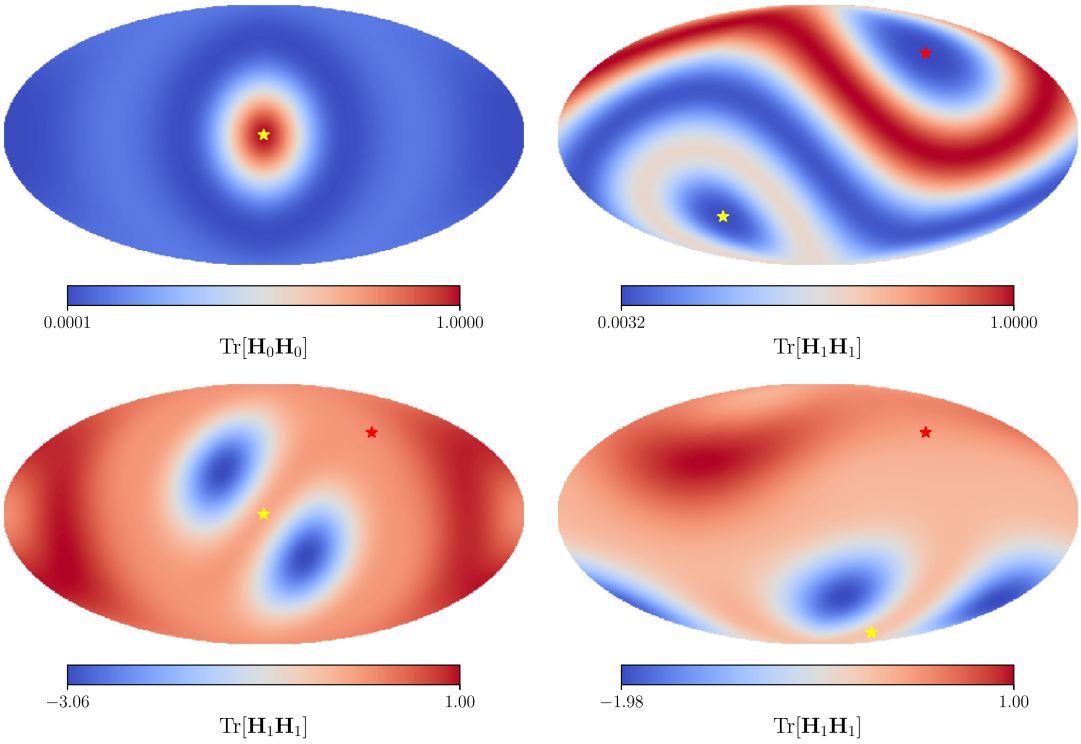

FIG. 1. Quantities $\mathrm{Tr}[\boldsymbol{H}_0\boldsymbol{H}_0]$ and $\mathrm{Tr}[\boldsymbol{H}_1\boldsymbol{H}_1]$, associated with the response to a SGWB depending on stars positions. (See the main text for our notation.) Motivated by CMB, we choose the kinematic dipole direction $\mathbf{v}$ (red star) at $(l, b) = (264°, 48°)$ in galactic coordinates. Each panel shows a different choice of $\mathbf{n}$, while the stars $\mathbf{q}$ take the position of each pixel of the map. Upper left panel: $\mathbf{n}$ pointing toward $(l, b) = (0, 0)$. Upper right panel: $\mathbf{n}$ pointing toward $-\mathbf{v}$. Lower left panel: $\mathbf{n}$ at $(l, b) = (0, 0)$. Lower right panel: $\mathbf{n}$ pointing toward the direction $(l, b) = (270.21°, -75.45°)$.

$$a_2 = \frac{\pi[(y-1)(2y+1) - 3y\ln(y)][2(nv)(1-y) + \sqrt{4(1-nv)^2(1-y)y - (Av)^2}]}{6(1-y)^3}. \tag{2.20}$$

Our analytical, covariant expression (2.17) for the ORF demonstrates that the astrometry sensitivity to the SGWB dipole depends not only on the angle among stars, ζ, but also on their position in the sky, and on the velocity vector $\mathbf{v}$ among frames.

The compact expressions (2.15) and (2.17) are particularly suitable to visualize patterns of sensitivity on the celestial sphere, and to further explore geometrical features of physically relevant quantities in the context we are examining. We plot in Fig. 1 the combinations.

$\mathrm{Tr}[\boldsymbol{H}_0\boldsymbol{H}_0]$ and $\mathrm{Tr}[\boldsymbol{H}_1\boldsymbol{H}_1]$ are representative of the sensitivity of astrometry observations to the monopole (through the function $\boldsymbol{H}_0$) and the dipole (through the function $\boldsymbol{H}_1$).[3] (Further theoretical motivations for considering such combinations are developed in Sec. III.) We introduce here the shorthand notation $\boldsymbol{H}_{0,1}$ to more compactly express the matrices involved with components $H_{ij}^{(0,1)}$. The quantity $\mathrm{Tr}[\boldsymbol{H}_0\boldsymbol{H}_0]$ does not depend on the velocity $\mathbf{v}$ among frames, and its magnitude depends only on the angle ζ between the stars, as defined in Eq. (2.14). (See also Appendix B for analytical expressions of the combinations we plot.) In the upper left panel of Fig. 1, we analyze the quantity $\mathrm{Tr}[\boldsymbol{H}_0\boldsymbol{H}_0]$ in the case where one of the star directions $\mathbf{n}$ points to the center of the sky map; the function reaches its local maxima at $\zeta = 0°$ and $\zeta \approx 105.6°$, and has two roots at $\zeta = 180°$ and $\zeta \approx 57.10°$. Such features are also represented on the left panel of Fig. 2. Next, the quantity $H_{ij}^{(1)}$ controls the sensitivity to the kinematic dipole and depends not only on the angle between the stars but also on the angle between the velocity $\mathbf{v}$ and the stars' directions; see Eq. (2.17). In the lower panels of Fig. 1, we present two maps to represent the properties of this function. Complex patterns for the ORF sensitivity to GW arise, depending on the direction of star positions in the sky. Nevertheless, we can consider a simple scenario where $\mathbf{n}$ is parallel to $\mathbf{v}$. This assumption simplifies

[3]A dipolar anisotropy also induces a correlation between the electric E and magnetic B components of the angular deflection correlation functions. We explore this topic in Appendix A.

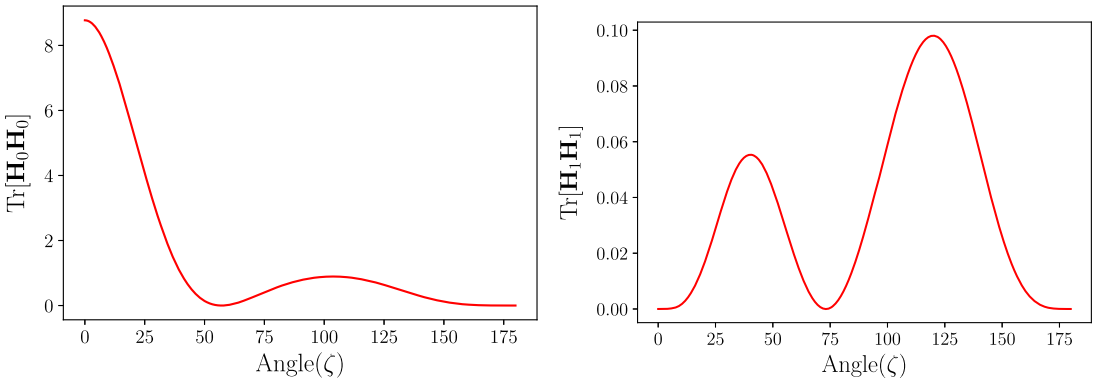

FIG. 2. Overlap functions' response in terms of the angle between the stars. Left panel: angular dependence for $\mathrm{Tr}[\boldsymbol{H}_0\boldsymbol{H}_0]$. Right panel: $\mathrm{Tr}[\boldsymbol{H}_1\boldsymbol{H}_1]$ when choosing $\mathbf{n} = -\mathbf{v}$.

the expression for $\mathrm{Tr}[\boldsymbol{H}_1\boldsymbol{H}_1]$ and allows us to appreciate the system sensitivity to SGWB properties only in terms of the angle separation ζ among the stars. In the upper right panel of Fig. 1, the red band represents the regions of higher sensitivity. The maximum of the function is reached at $\zeta \approx 119.45°$, while the blue regions represent the lowest values of the function, including its three roots at $\zeta = 0, \pi$ and $\zeta \approx 73.14°$. The resulting behavior is also represented in the right panel of Fig. 2.

B. Cross-correlated overlap functions of astrometry and PTA

In the future, precise astronomical observations will improve astrometry measurements, making them more sensitive to GW. The synergy of astrometry and PTA will be instrumental for increasing the sensitivity to the properties of the SGWB. It is therefore important to analytically compute the overlap functions associated with cross-correlations between astrometry deflections and pulsar timings, also including effects of SGWB anisotropies. These topics have been explored in [28,29,31]. We present here covariant expressions for the overlap functions of cross-correlations, which are convenient for numerical analysis and for the forecasts we carry out in Sec. III.

We consider two-point correlation functions of deflections of star positions and of pulsar time delays $z(t) = \Delta T(t)/T(t)$, where $T(t)$ is the total time the radio signal needs for traveling from the pulsar source to the detector. We denote with $\mathbf{x}$ the unit vector pointing from the Earth toward the specific pulsar being monitored. The time delay induced by a GW propagating along the direction $\mathbf{p}$ results (see e.g., [93]) in

$$z(t) = \frac{1}{2}\frac{x^i x^j}{1+\mathbf{x}\cdot\mathbf{p}} h_{ij}(t,0), \tag{2.21}$$

where we include the Earth term only [93]. This information, together with the results of Sec. II A, allows us to compute the correlation functions between star deflection $\delta n^i(\mathbf{n},t)$ and $z(t)$, induced by the presence of a SGWB. It reads

$$\langle \delta n_i(\mathbf{n},t) z(t)\rangle = \frac{3H_0^2}{64\pi^3}\int df \frac{\bar{\Omega}_{\mathrm{GW}}(f)}{f^3} \times [K_i^{(0)}(\mathbf{n},\mathbf{x}) + \beta(4-n_\Omega)K_i^{(1)}(\mathbf{n},\mathbf{x},\mathbf{v})]. \tag{2.22}$$

In analogy with the formulas developed in Sec. II A, the quantities $K_i^{(0)}$ and $K_i^{(1)}$ denote, respectively, the cross-correlated overlap reduction functions relative to the SGWB monopole and kinematic dipole. Using the same notation of the previous section, they are expressed in terms of the angular integrals

$$K_i^{(0)}(\mathbf{n},\mathbf{x}) = \int d^2\Omega_{\mathbf{p}}\, \mathcal{R}_{ikl}(\mathbf{n},\mathbf{p}) P_{klrs}\frac{x^r x^s}{1+\mathbf{x}\cdot\mathbf{p}}, \tag{2.23}$$

$$K_i^{(1)}(\mathbf{n},\mathbf{x},\mathbf{v}) = \int d^2\Omega_{\mathbf{p}}(\mathbf{p}\cdot\mathbf{v})\mathcal{R}_{ikl}(\mathbf{n},\mathbf{p}) P_{klrs}\frac{x^r x^s}{1+\mathbf{x}\cdot\mathbf{p}}. \tag{2.24}$$

These integrals can be computed straightforwardly through contour integration in the complex plane. It is convenient to express the results in terms of the quantity [not to be confused with the analogous quantity (2.14) of Sec. II A]

$$y = \frac{1-\mathbf{n}\cdot\mathbf{x}}{2}, \tag{2.25}$$

related to the angle between the direction of the monitored star and pulsar. The ORF of the cross-correlation monopole reads

$$K_i^{(0)}(\mathbf{n},\mathbf{x}) = \frac{16\pi}{3}\frac{(1-2y)n_i - x_i}{4y(1-y)}(2y - 2y^2 + 3y^2\ln(y)), \tag{2.26}$$

a formula equivalent to the one found in [28], although expressed in another form.

The overlap function for the kinematic dipole is more easily expressed in terms of two vectors $\mathbf{A}_{1,2}$ orthogonal to the star direction $\mathbf{n}$:

$$\mathbf{A_1} = \mathbf{n} \times \mathbf{x}, \tag{2.27}$$

$$\mathbf{A_2} = \mathbf{n} \times \mathbf{v}. \tag{2.28}$$

Notice the identity $\mathbf{A_1} \cdot \mathbf{A_2} = \mathbf{x} \cdot \mathbf{v} - (\mathbf{n} \cdot \mathbf{v})(\mathbf{n} \cdot \mathbf{x})$. We parametrize the dipolar overlap function as

$$K_i^{(1)}(\mathbf{n}, \mathbf{x}, \mathbf{v}) = b_1 A_{1i} + b_2 A_{2i}. \tag{2.29}$$

We denote $\mathbf{A_1} \cdot \mathbf{v} = (A_1 v)$, etc. The two coefficients $b_{1,2}$ can be computed by contour integration,[4]

$$b_1 = \frac{\pi((A_1v)^2(1-12y) + (A_1A_2)((A_1A_2) + 12(A_1A_2)y^2 + 4(nv)y(1+y(5-6y))))}{6(A_1v)(1-y)y} + \frac{2\pi((A_1A_2)^2 - (A_1v)^2 + 2(A_1A_2)(nv)(1-y))y\ln(y)}{(A_1v)(1-y)^2}, \tag{2.31}$$

$$b_2 = -\frac{2\pi((A_1A_2) + 12(A_1A_2)y^2 + 4(nv)y(1+y(5-6y)))}{3(A_1v)} - \frac{8\pi((A_1A_2) + 2(nv)(1-y))y^2\ln(y)}{(A_1v)(1-y)}. \tag{2.32}$$

Analogously to our discussion toward the end of Sec. II A, we can visualize the ORF for astrometry working in synergy with PTA experiments. They are controlled by the combinations $\mathbf{K}_0\mathbf{K}_0^T$ and $\mathbf{K}_1\mathbf{K}_1^T$. We denote the vectors $K_i^{(0,1)} \equiv \mathbf{K}_{0,1}$ more compactly.

We call ζ_{sp} the angle between the star and pulsar directions, $\cos\zeta_{sp} = \mathbf{n} \cdot \mathbf{x}$. We represent a simple example in the upper left panel of Fig. 3 with $\mathbf{n}$ pointing toward $(l, b) = (0, 0)$; the roots of the function $\mathbf{K}_0\mathbf{K}_0^T$ are at $\zeta_{sp} = 0, \pi$ and $\zeta_{sp} \approx 86.14°$, while its local maxima are located at $\zeta_{sp} \approx 37.13°$ and $\zeta_{sp} \approx 132.195°$, and are represented in the left panel of Fig. 4. The lower panel of Fig. 3 shows two scenarios for the general expression for the function $\mathbf{K}_1\mathbf{K}_1^T$ (see also Appendix B), which depends on the angle between the star and pulsar and the angle between the velocity and pulsars given by $vx = \mathbf{v} \cdot \mathbf{x}$; on the left, we choose $\mathbf{n}$ at $(l, b) = (0, 0)$, and on the right, $\mathbf{n}$ is at position $(l, b) = (270.21°, -75.45°)$ (a direction chosen randomly). The sensitivity patterns are complex. However, in the specific case of the star direction $\mathbf{n}$ pointing toward the direction $-\mathbf{v}$, we obtain a simple formula, depending only on the angle between the star and pulsar. This last case is shown on the right upper panel of Fig. 3, where the bluest, less sensitive regions show the positions of objects at relative angles $\zeta_{sp} = 0, \pi$ and 39.82°, 101.37°, corresponding to minimal sensitivity to the dipole. The red region shows the positions of the pulsars where the function $\mathbf{K}_1\mathbf{K}_1^T$ reaches its maximum at $\zeta_{sp} \approx 142.29°$. There are also local maxima at $\zeta_{sp} \approx 17.97°, 71.88°$, which are more apparent on the right panel of Fig. 4. Notice that the quantities $\mathbf{K}_{0,1}$ corresponding to the synergetic ORF vanish in the coincident limit of the star aligned with the pulsar direction. One may understand this as follows—the star deflection always lies in the plane perpendicular to the line of sight. On the contrary, the pulsar timing residual arises from the change in length along the line of sight. Thus, for a pulsar and star in the same direction, the two effects are perpendicular to each other.

III. FISHER FORECASTS

Armed with the covariant, analytical expressions we derived for the ORF of astrometry and PTA systems—including the effects of kinematic anisotropies—in this section, we investigate the prospects of future experiments to characterize the SGWB. We are interested in measuring the SGWB amplitude and its spectral tilt, as well as the magnitude of a possible dipolar anisotropy characterizing the SGWB. We quantify how the results depend on the number of astronomical objects we measure, as well as on the precision of their measurement.

In this section, we use the Fisher matrix approach to forecast the sensitivity of astrometry, individually and jointly with PTA, to the SGWB properties, such as the

[4]The expression (2.29) is valid for all values of angles among the vectors involved, apart from when $\mathbf{n} \cdot \mathbf{v} = 0$. Then, the vector $\mathbf{A}_2$, as well as the product $\mathbf{A}_1 \cdot \mathbf{v}$, vanishes. The limit $\mathbf{n} \cdot \mathbf{v} \to 0$ is hence delicate. For this specific case of velocity vector $\mathbf{v}$ parallel to the star direction $\mathbf{n}$, the expression for the dipole response function reduces to

$$K_i^{(1)}(\mathbf{n}, \mathbf{x}) = \frac{2\pi(n_i(1-2y) - x_i)}{3(1-y)}((y-1)(6y+1) - 6y\ln(y)). \tag{2.30}$$

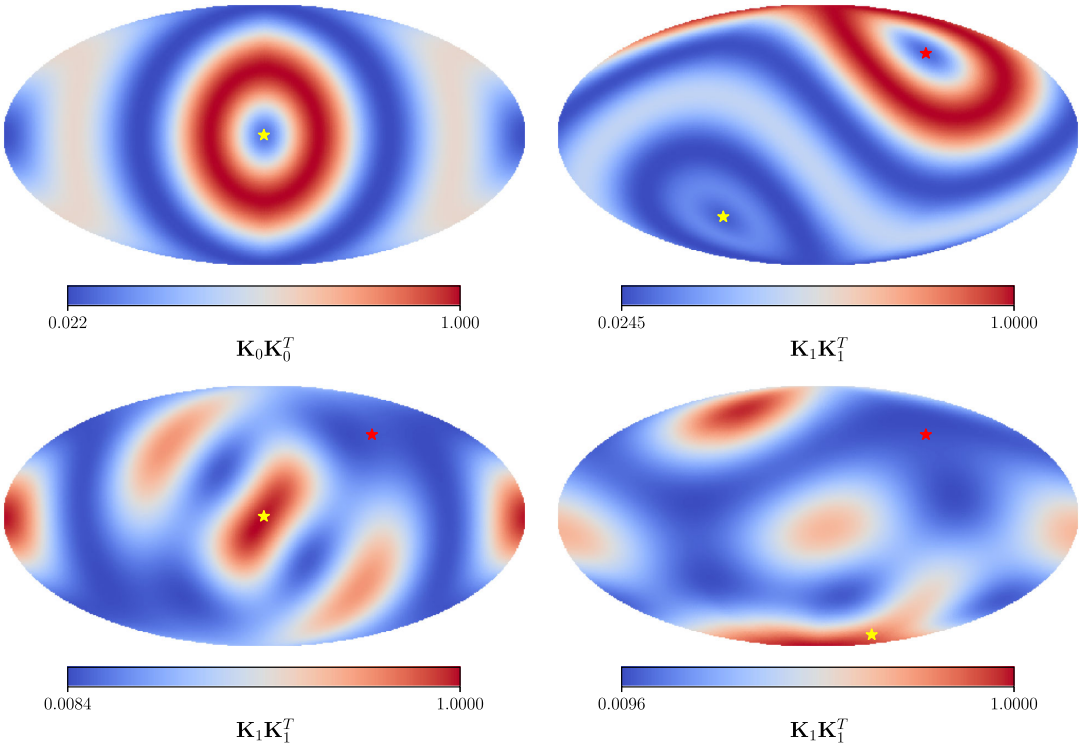

FIG. 3. Response of the quantities $\mathbf{K}_0\mathbf{K}_0^T$ and $\mathbf{K}_1\mathbf{K}_1^T$ to star and pulsar positions. The dipole direction $\mathbf{v}$ (red star) is chosen in the direction $(l, b) = (264°, 48°)$ in galactic coordinates. Each panel shows a different choice of $\mathbf{n}$, while the pulsar positions $\mathbf{x}$ scan over each pixel of the map. Upper left panel: $\mathbf{n}$ toward $(l, b) = (0, 0)$. Upper right panel: $\mathbf{n}$ toward $-\mathbf{v}$. Lower left panel: $\mathbf{n}$ at $(l, b) = (0, 0)$. Lower right panel: $\mathbf{n}$ toward $(l, b) = (270.21°, -75.45°)$.

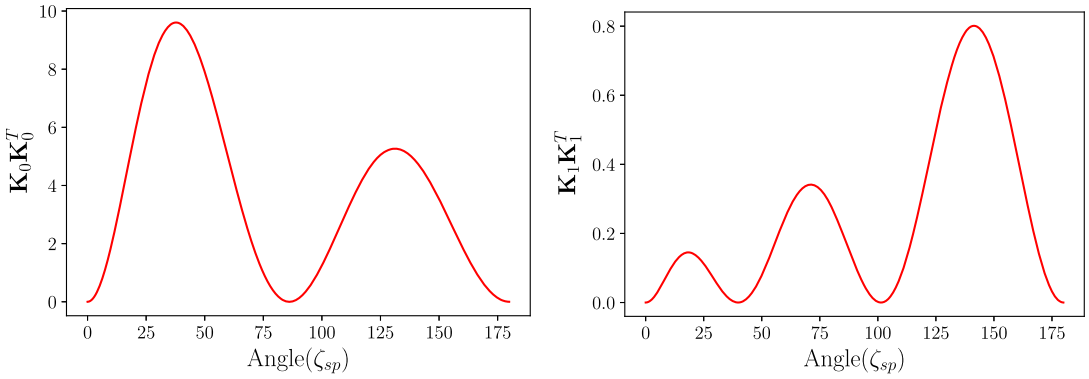

FIG. 4. Overlap function response in terms of the angle between the stars and pulsars. Left panel: angular dependence for $\mathbf{K}_0\mathbf{K}_0^T$. Right panel: quantities $\mathbf{K}_1\mathbf{K}_1^T$ when choosing $\mathbf{n} = -\mathbf{v}$.

amplitude, spectral index, and dipole anisotropy. In appropriate limits and special cases, the Fisher matrix obeys interesting scaling relations which make our analysis particularly simple. In general though, numerical work is needed to evaluate to what extent the synergy between astrometry and PTA improve the sensitivity to SGWB properties. We carry out such an analysis in Secs. III A, III B, and III B 3, making use of the weak-signal approximation for astrometry to simplify the numerical calculations for a large number of stars.

A. Astrometry only

We start by discussing the case of astrometry only. We expand the deflection correlation of Eq. (2.9) in a basis with coefficients p_n,[5]

[5]In principle, these basis coefficients can also be spherical harmonics coefficients or individual pixels used to discretize the SGWB intensity map. Our analysis represents a special case where we only expand the SGWB intensity up to the dipole term, assuming a known dipole direction.

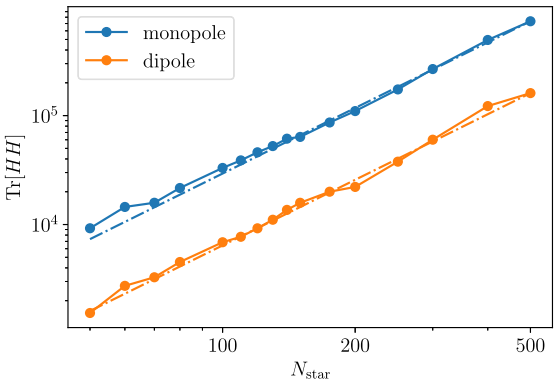

FIG. 5. Components of the Fisher matrix (3.13) evaluated numerically as a function of the number of stars, with the stars uniformly distributed across the sky. The dashed lines have slope N_{star}^2 and pass through the numerically evaluated result for $N_{\mathrm{star}} = 500$. This plot numerically confirms Eqs. (3.14) and (3.15).

$$\langle \delta n_a^i \delta n_b^j \rangle \equiv C_{ab}^{ij} = \sum_{n=0,1} p_n H_{ab,n}^{ij} + N_{ab}^{ij}. \tag{3.1}$$

The indices a, b identify the two stars, and i, j are the three-dimensional vector components. The index n runs over 0,1, indicating monopolar and dipolar contributions to the signal. We include the effects of noise through the noise matrix N_{ab}^{ij}. The quantities p_n and $H_{ab,n}$ are controlled by the properties of the SGWB, as well as the astrometry ORF. See Eq. (2.9) and the discussion that follows for the definitions. The angle brackets on the lhs denote the expectation value of the correlation of the ith deflection of star a with the jth deflection of star b. To keep our notation compact, we now use bold symbols to represent the signal covariance as well as the noise matrix, i.e.,

$$C_{ab}^{ij} \equiv \mathbf{C} = \sum_{n=0,1} p_n H_{ab,n}^{ij} + N_{ab}^{ij} \equiv \sum_{n=0,1} p_n \boldsymbol{H}_n + \boldsymbol{N}. \tag{3.2}$$

Thus, in the following, the trace of the product of two bold quantities represents a sum over the i, j and a, b indices, i.e.,

$$\mathrm{Tr}[\boldsymbol{AB}] = \sum_{ij,ab} A_{ab}^{ij} B_{ab}^{ij}. \tag{3.3}$$

At this stage, we do not need to specify whether we work in time or in frequency domains.

Our aim is to determine how well we can measure the quantities $p_{0,1}$ and extract from this information about the properties of the SGWB: its monopole amplitude Ω_{GW} as well as the value of the parameter β controlling kinematic anisotropies, using a Fisher matrix approach.[6]

[6]We also discuss the optimal estimators for the SGWB monopole and dipole in Sec. C.

However, before proceeding to build the Fisher matrix for the monopole and dipole amplitudes, we note that the matrix C cannot directly be used as a covariance matrix since it is singular. This stems from the fact that the three Cartesian deflection components are not independent since observations get projected onto the two-dimensional celestial sphere. Hence, the star deflections can be entirely described in terms of two angles, $\delta\theta$ and $\delta\phi$ [28]. Let P be the matrix that converts the deflections from 3D Cartesian to 2D polar coordinates, i.e.,

$$\begin{pmatrix} \delta\theta \\ \delta\phi \end{pmatrix} = P \cdot \begin{pmatrix} \delta x \\ \delta y \\ \delta z \end{pmatrix}. \tag{3.4}$$

The matrix P is used to convert the original correlation matrix for the Cartesian deflections to a correlation matrix in terms of angular deflections. For a single star, it is given by [28]

$$P = \begin{bmatrix} 0 & 0 & \frac{1}{\sqrt{1-z^2}} \\ -\frac{y}{x^2+y^2} & \frac{x}{x^2+y^2} & 0 \end{bmatrix}. \tag{3.5}$$

For the full system of N stars, the projection matrix R can be written in block diagonal form [28],

$$R = \begin{bmatrix} P_1 & 0 & \dots & 0 \\ 0 & P_2 & \dots & 0 \\ \vdots & \vdots & \ddots & \vdots \\ 0 & 0 & \dots & P_n \end{bmatrix}. \tag{3.6}$$

This can be used to obtain the angular deflection covariance matrix from the Cartesian one

$$C_{ij}^{\delta\vec{\theta}} = R \cdot C_{ij}^{\delta\vec{x}} \cdot R^T, \tag{3.7}$$

which is the actual covariance matrix that will be used for the calculations that follow. For zero mean, Gaussian-distributed astrometric deflections, the likelihood $\mathcal{L}$ takes the form

$$-2 \ln \mathcal{L} = \delta n_a^i [C^{-1}]_{ab}^{ij} \delta n_b^j + \ln \det \mathbf{C} + n \ln 2\pi. \tag{3.8}$$

How well we can determine the parameters that describe our signal is controlled by the Fisher matrix, defined as [99]

$$\mathcal{F}_{ij} = \left\langle -\frac{\partial \ln \mathcal{L}}{\partial\theta_i \partial\theta_j} \right\rangle, \tag{3.9}$$

given in terms of the expectation value of second derivatives of $\ln \mathcal{L}$. The Fisher matrix sets a lower bound on the

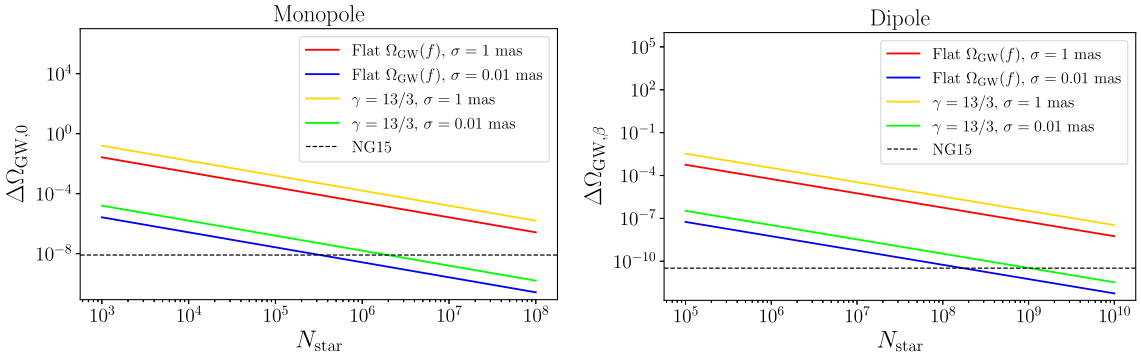

FIG. 6. Forecasts for the magnitude of the SGWB energy density and dipolar anisotropy, as measured with astrometry. See the discussion after Eq. (3.15). Left panel: error $\Delta\Omega_{\rm GW,0}$ associated with the monopole estimator p_0. Right panel: $\Omega_{{\rm GW},\beta}$ associated with the dipole estimator p_1. We define $\Omega_{{\rm GW},\beta} = \beta(4 - n_\Omega)\Omega_{\rm GW,0}$. The dashed lines correspond to $\Delta\Omega_{\rm GW,0} \approx 8.05 \times 10^{-9}$, which is the value of the energy density with the NG15 results [100], and $\Delta\Omega_{{\rm GW},\beta} \approx 3.3 \times 10^{-11}$.

precision with which these parameters can be measured, $\Delta\theta_{i,\rm min} = \sqrt{[\mathcal{F}^{-1}]_{ii}}$. For the likelihood in (3.8), the Fisher matrix reads [99]

$$\mathcal{F}_{ij} = \frac{1}{2}{\rm Tr}[C^{-1}C_{,i}C^{-1}C_{,j}], \tag{3.10}$$

where $C_{,i}$ denotes the derivative of C with respect to the parameter θ_i. Using the definition of the covariance (3.1), we see that

$$C_{,i} = \sum_n \frac{\partial p_n}{\partial\theta_i}\boldsymbol{H}_n. \tag{3.11}$$

Specializing to the case where our signal parameters θ_i correspond to the monopole and dipole amplitude p_0 and p_1 as in Eq. (3.1), the Fisher matrix reads

$$\mathcal{F}_{ij} = \frac{1}{2}{\rm Tr}[C^{-1}H_iC^{-1}H_j], \tag{3.12}$$

where i, j run from 0 to 1. In the noise-dominated limit with a diagonal noise covariance matrix $N^{ij}_{ab} = \sigma_N^2\delta_{ab}\delta^{ij}$, we obtain the Fisher matrix $\mathcal{F}$ for p_0, p_1 as

$$\mathcal{F} = \frac{1}{2\sigma_N^4}\begin{pmatrix} {\rm Tr}[\boldsymbol{H}_0\boldsymbol{H}_0] & {\rm Tr}[\boldsymbol{H}_0\boldsymbol{H}_1] \\ {\rm Tr}[\boldsymbol{H}_0\boldsymbol{H}_1] & {\rm Tr}[\boldsymbol{H}_1\boldsymbol{H}_1] \end{pmatrix}. \tag{3.13}$$

Hence, in the noise-dominated regime, the Fisher matrix depends only on the ORF of the monopole and dipole of the SGWB, discussed in Sec. II.

The entries of the Fisher matrix (3.13) simplify under certain hypotheses. For example, we find the following scaling relations which hold in the limit of large $N_{\rm star} \gg 100$ stars distributed uniformly across the sky (see Fig. 5):

$$\mathcal{F}_0 \equiv {\rm Tr}[\boldsymbol{H}_0\boldsymbol{H}_0] \simeq 3 \times N_{\rm star}^2, \tag{3.14}$$

$$\mathcal{F}_1 \equiv {\rm Tr}[\boldsymbol{H}_1\boldsymbol{H}_1] \simeq 0.65 \times N_{\rm star}^2. \tag{3.15}$$

In the same limit, the cross terms depending on ${\rm Tr}[\boldsymbol{H}_0\boldsymbol{H}_1]$ vanish in Eq. (3.13). In practice, to perform Fisher forecasts by means of Eq. (3.13), we focus on the frequency domain, performing a frequency binning with $\Delta f = 1/T_{\rm obs}$, with $T_{\rm obs} = 15$ years, and summing over the Fisher matrices at each frequency bin. We relate the value of the GW energy density $\Omega_{\rm GW}$ to the intensity through Eq. (2.7). We assume for the latter a power-law ansatz $I(f) = I_0(f/f_*)^{2-\gamma}$ and report our results in Fig. 6 for different values of spectral slope, also showing the detection threshold indicated by the IPTA joint analysis [9].

The noise in the frequency domain is given by $\sigma_N^2(f) = 2\sigma^2 T_{\rm cad}$, where we have assumed a white noise component only. We take different values of σ as shown in Fig. 6 and the observational cadence $T_{\rm cad} = {\rm year}/15$, corresponding approximately to the observational cadence of Gaia [36]; i.e., $T_{\rm cad}$ represents the time interval (in seconds) between successive observations of a particular star.

Assuming noise-dominated covariance, the uncertainties for the intensity monopole amplitude I_0 and the dipole amplitude $I_\beta \equiv (1 - n_I)\beta I_0$[7] take the following form:

$$\mathcal{F}_{I_0I_0} = \frac{T_{\rm obs}}{2\sigma_N^4}\frac{{\rm Tr}[\boldsymbol{H}_0\boldsymbol{H}_0]}{(4\pi)^2}\sum_f (f/f_*)^{2n_I}\Delta f, \tag{3.16}$$

$$\mathcal{F}_{I_\beta I_\beta} = \frac{T_{\rm obs}}{2\sigma_N^4}\frac{{\rm Tr}[\boldsymbol{H}_1\boldsymbol{H}_1]}{(4\pi)^2}\sum_f (f/f_*)^{2n_I}\Delta f, \tag{3.17}$$

with $n_I = 2 - \gamma$. To obtain a scaling relation, we replace the discrete sum by an integral,

$$\sum_f (f/f_*)^{2n_I}\Delta f \approx \int_{f=1/T_{\rm obs}}^{1/T_{\rm cad}} (f/f_*)^{2n_I} df. \tag{3.18}$$

[7]Note the relation $n_\Omega = n_I + 3$ arising from (2.7).

Given that $n_I = -7/3 < 0$,[8] the integral is dominated by the lower frequencies and can be approximated (for $n_I \neq -1/2$) by

$$\left[\int_{f=1/T_{\rm obs}}^{1/T_{\rm cad}} (f/f_*)^{2n_I} df\right] \approx \left[-\frac{f_{\rm min}}{2n_I+1}\left(\frac{f_{\rm min}}{f_*}\right)^{2n_I}\right]. \quad (3.19)$$

Since, for a given parameter θ, $\Delta\theta = \sqrt{[\mathcal{F}^{-1}]_{\theta\theta}}$, we obtain

$$\Delta I_0 = \sqrt{\frac{2}{3|2n_I+1|}}\frac{4\pi\sigma_N^2}{N_{\rm star}}\left(\frac{T_{\rm obs}}{1\ \text{year}}\right)^{n_I}, \quad (3.20)$$

$$\Delta I_\beta = \sqrt{\frac{2}{0.65|2n_I+1|}}\frac{4\pi\sigma_N^2}{N_{\rm star}}\left(\frac{T_{\rm obs}}{1\ \text{year}}\right)^{n_I}, \quad (3.21)$$

where we used the fact that $f_{\rm min} = 1/T_{\rm obs}$ and $f_* = 1/\text{year}$. Using the relation between the intensity and energy density (2.7) allows us to convert these expressions to uncertainties in $\Omega_{\rm GW}$. We find

$$\Delta\Omega_{{\rm GW},0(\beta)} = 1.6(3.4)\times 10^{-8}\sqrt{\frac{|2n_I+1|}{4/3}}\left(\frac{\sigma}{0.01}\right)^2 \times \left(\frac{T_{\rm cad}}{\text{year}/15}\right)\left(\frac{10^6}{N_{\rm star}}\right)\left(\frac{T_{\rm obs}}{15\ \text{year}}\right)^{n_I}. \quad (3.22)$$

We emphasize that these relations hold only in the noise-dominated (weak-signal) limit and for sufficiently red-tilted SGWB, assuming that this tilt is known and not itself being inferred from the data.

Under the assumptions leading to Eqs. (3.14) and (3.15), we find that astrometric surveys with 0.01 milli-arcsecond (mas) precision which monitor $N > 10^6$ stars may be competitive with PTA experiments, in terms of sensitivity to the SGWB. The detection of the kinematic dipole, whose amplitude is suppressed by a factor β relative to the monopole, will accordingly require about 10^3 times more stars. We should note, though, that for the green and blue lines shown in Fig. 6, the weak-signal approximation likely breaks down as we go toward a higher and higher number of stars ($N_{\rm star} \gg 10^6$). The noise level $\sigma = 0.01$ mas roughly corresponds to the expected astrometric accuracy that will be achieved by Gaia DR5 for the brightest objects in the survey.[9] Thus, the forecast sensitivity with this value of the noise is very unlikely to be achieved in real Gaia DR5 data but may be possible with future missions like Theia [48–50].

[8]The fiducial value $n_I = -7/3$ adopted here corresponds to the theoretical expectation for supermassive black hole binaries in circular orbits [101].

[9]https://www.cosmos.esa.int/web/gaia/science-performance.

B. Forecasts: Astrometry in synergy with PTA

We now turn our attention to estimators and forecasts for astrometry in synergy with PTA. In this section, we consider only the isotropic part of the background, focusing on the amplitude and spectral tilt of the SGWB. The effect of the kinematic dipole is investigated in Sec. III B 3.

Let $\delta t_a, a = 1, 2, \ldots N$, and $\delta\vec{\theta}_b, b = 1, 2, \ldots M/2$ be the Fourier transforms of timing residuals and angular deflections of N pulsars and $M/2$ stars, respectively.[10] We work under the assumption of a Gaussian-distributed SGWB with zero mean. The joint covariance matrix at a given frequency can be written in block form as

$$C_{(N+M)\times(N+M)} = \begin{bmatrix} A_{N\times N} & B_{N\times M} \\ B^T_{M\times N} & D_{M\times M}\end{bmatrix}, \quad (3.23)$$

and the joint likelihood can be written as

$$-2\ln L = (\vec{\delta t}, \vec{\delta\theta})\cdot C^{-1}\cdot(\vec{\delta t}, \vec{\delta\theta}))^T + \ln\ \det\ C + \frac{(M+N)}{2}\ln 2\pi. \quad (3.24)$$

As explained previously, we split the total frequency interval we analyze into frequency bins.

The individual submatrices A, B, D denote the pulsar-pulsar, pulsar-star, and star-star covariance matrices, respectively. Notice that they have very different dimensionalities since we expect to monitor many more stars than pulsars (more on this later). They read

$$A_{pq} = \frac{\gamma_{pq} I_f}{(4\pi f)^2} + \sigma_p^2\delta_{pq}, \quad (3.25)$$

$$B_{pa} = \frac{K_{p,a} I_f}{(4\pi)^2 f}, \quad (3.26)$$

$$D_{ab} = \frac{H_{ab}}{4\pi} I_f + \delta_{ab}\sigma_a^2. \quad (3.27)$$

The tensor γ_{pq} corresponds to the HD interpulsar correlation between pulsar time delays,[11] while $K_{p,a}$ and H_{ab} denote the pulsar-star and star-star correlations studied in Sec. II. In general, the covariance matrices depend explicitly on the SGWB intensity I_f evaluated at the frequency bin under examination. (We use the same notation as [102,103].)

The Fisher matrix for the joint forecast is given by the usual formula [104]

[10]The factor of 2 arises for the stars because they are each characterized by two angular deflections in the sky, while pulsars are only characterized by a single time delay.

[11]For the HD correlations, we adopt the normalization convention of [84] where $\gamma_{pp} = 4/3$.

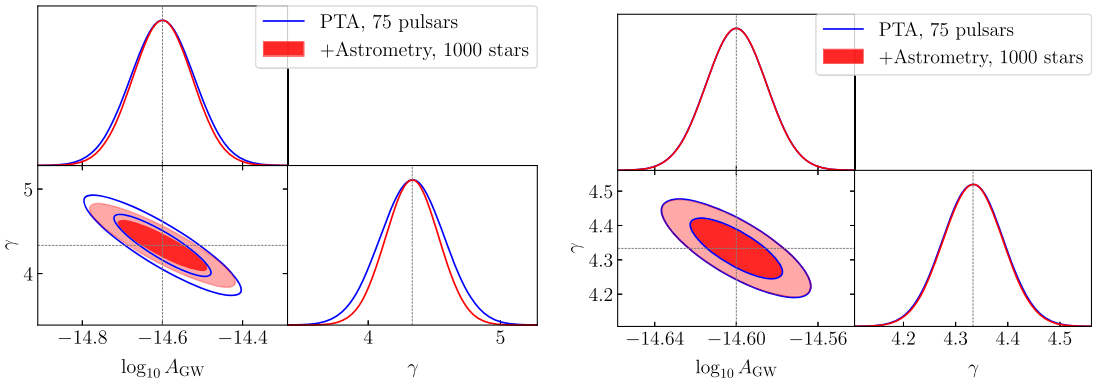

FIG. 7. Fisher forecast for Case 1 (left) and Case 2 (right) in Sec. III B 1.

$$\mathcal{F}_{\alpha\beta} = \frac{1}{2}\mathrm{Tr}[C^{-1}C_\alpha C^{-1}C_\beta], \tag{3.28}$$

where C_α denotes the derivative with respect to the parameter α. We wish to investigate how the addition of the astrometric datasets can help to improve upon the constraints on the SGWB amplitude and spectral tilt, with respect to an analysis based only on PTA data.

We first calculate the inverse of our covariance matrix. When the matrices A and D are both invertible, as is the present case, the inverse is given by [105,106]

$$C^{-1} = \begin{bmatrix} (A - BD^{-1}B^T)^{-1} & 0 \\ 0 & (D - B^TA^{-1}B)^{-1} \end{bmatrix} \times \begin{bmatrix} \mathbb{1}_N & -BD^{-1} \\ -B^TA^{-1} & \mathbb{1}_M \end{bmatrix}, \tag{3.29}$$

while the derivative C_α reads

$$C_\alpha = \begin{bmatrix} A_\alpha & B_\alpha \\ B_\alpha^T & D_\alpha \end{bmatrix}. \tag{3.30}$$

1. Some concrete examples

To demonstrate how the cross-correlation of astrometric and PTA data can be useful to characterize the SGWB signal—even when the astrometric data alone are not very constraining—we start with a simple toy example.

Case 1: We parametrize the SGWB intensity as

$$I(f) = \frac{A_{\rm GW}^2}{2f_{\rm ref}}\left(\frac{f}{f_{\rm ref}}\right)^{2-\gamma}, \tag{3.31}$$

using the quantities $A_{\rm GW}$ and γ to make comparison with PTA analyses simpler,[12] with $f_{\rm ref} = 1/\mathrm{year}$. We choose PTA parameters so as to recover the level of constraints set by the IPTA joint analysis [9] with 15 years of observation time, roughly corresponding to $\log_{10} A_{\rm GW} = -14.6 \pm 0.16, \gamma = 13/3 \pm 0.45$ at 95% C.L. For the astrometric analysis, we take 1000 stars with identical noise level $\sigma_S^2 = 2[\Delta\theta_{\rm rms}]^2 T_{\rm cad}$ with $\Delta\theta_{\rm rms} = 0.0002$ mas and $T_{\rm cad} = \mathrm{year}/52$, i.e., with each star observed once per week.

Although these numbers are not representative of typical astrometric datasets, which have a larger number of stars and at the same time larger noise levels, this toy example suffices to make our point and is computationally feasible without making any approximations for the Fisher matrix. Both the pulsar and the star configuration should be distributed uniformly across the sky.

In the left panel of Fig. 7, we plot the Fisher forecast for the parameters $\log A_{\rm GW}$ and γ within this setup. We learn that the joint PTA + Astrometric dataset provides an improvement over the PTA-only constraints, even when the astrometric data alone are not too informative.

Case 2: We proceed by presenting one more example, plotted in the right panel of Fig. 7, keeping the same noise properties for the astrometry set but with the PTA system in the strong-signal (noiseless) regime. We see that the improvement in constraints with the addition of astrometry can be sizable if the PTA datasets are not in the strong signal regime; however, it is much smaller if that is indeed the case.

2. Method for handling large Fisher matrices

In the examples discussed above, we are able to perform the necessary computations involving Fisher matrices and their inversion, given the relatively small size of astrometric covariance matrix involved. However, for realistic datasets which may contain over 10^6 stars, inverting matrices of such dimensionality can become demanding. To handle forecasts for such datasets, we develop a simple method to perform the Fisher forecasts in weak astrometric signal limits without needing to resort to the full numerical calculations. The weak-signal limit is justified since current astrometric datasets are very much in the noise-dominated

[12]We follow the conventions outlined in [102] to relate these quantities, where $h_c(f) \equiv \sqrt{2fI(f)} = A_{\rm GW}(f/f_{\rm ref})^\alpha$, with $\gamma \equiv 3 - 2\alpha$.

regime, and this is likely to be the case in the future as well.[13] Thus, we can approximate the matrix D of Eq. (3.27) as

$$D_{ij} \approx \delta_{ij}\sigma_i^2, \qquad [D^{-1}]_{ij} = \delta_{ij}\sigma_i^{-2}. \tag{3.32}$$

We further assume all stars have the same measurement noise $\sigma_i^2 = \sigma_S^2$, as well as identical noise for each pulsar σ_P^2.

In the noise-dominated approximation for the astrometric covariance, we write

$$C^{-1} = \begin{bmatrix} (A - B\sigma_S^{-2}\mathbb{1}_M B^T)^{-1} & 0 \\ 0 & (\sigma_S^2\mathbb{1}_M - B^T A^{-1} B)^{-1} \end{bmatrix} \times \begin{bmatrix} \mathbb{1}_N & -B\sigma_S^{-2}\mathbb{1}_M \\ -B^T A^{-1} & \mathbb{1}_M \end{bmatrix}. \tag{3.33}$$

Note that we do not assume a weak-signal limit for the pulsar covariance: In fact, we work with the full PTA covariance matrix. We focus on the relevant regime for PTA experiments since current measurements already suggest PTA measurements to lie in the intermediate signal regime—especially for the lower end of the frequency range. To evaluate the trace, we compute

$$C_\alpha C^{-1} = \begin{bmatrix} A_\alpha Q_1 & B_\alpha Q_2 \\ B_\alpha^T Q_1 & D_\alpha Q_2 \end{bmatrix} \begin{bmatrix} \mathbb{1}_N & -B\sigma_S^{-2}\mathbb{1}_M \\ -B^T A^{-1} & \mathbb{1}_M \end{bmatrix} = \begin{bmatrix} A_\alpha Q_1 - B_\alpha Q_2 B^T A^{-1} & -\sigma_S^{-2} A_\alpha Q_1 B + B_\alpha Q_2 \\ B_\alpha^T Q_1 - D_\alpha Q_2 B^T A^{-1} & -\sigma_S^{-2} B_\alpha^T Q_1 B + D_\alpha Q_2 \end{bmatrix}, \tag{3.34}$$

where

$$Q_1 = (A - B\sigma_S^{-2}\mathbb{1}_M B^T)^{-1}, \tag{3.35}$$

$$Q_2 = \sigma_S^{-2}(\mathbb{1}_M - \sigma_S^{-2} B^T A^{-1} B)^{-1}. \tag{3.36}$$

To proceed, we first note some useful relations involving the inverse of matrices

$$\left(A - B\frac{\mathbb{1}_M}{\sigma_S^2}B^T\right)^{-1} \approx \left[\mathbb{1}_N + \frac{A^{-1}BB^T}{\sigma_S^2} + \mathcal{O}(1/\sigma_S^4)\right]A^{-1}, \tag{3.37}$$

$$(D - B^T A^{-1} B)^{-1} \approx \frac{1}{\sigma_S^2}\left[\mathbb{1}_M + \frac{B^T A^{-1} B}{\sigma_S^2} + \mathcal{O}(1/\sigma_S^4)\right]. \tag{3.38}$$

[13]To be precise, this requires $MI(f) \ll 4\pi\sigma^2(f)$, where σ^2 denotes the frequency domain noise power spectral density. This condition ensures that the effect of the off-diagonal terms in the covariance is suppressed compared to the diagonal terms.

Then, we define $C_\alpha C^{-1} \equiv \mathcal{M}_\alpha$. For computing the trace in the expressions above, we need the diagonal elements of $\mathcal{M}_\alpha\mathcal{M}_\beta \equiv C_\alpha C^{-1} C_\beta C^{-1}$,

$$\mathcal{F}_{\alpha\beta} = \frac{1}{2}\mathrm{Tr}[\mathcal{M}_\alpha\mathcal{M}_\beta] = \frac{1}{2}\Big\{\underbrace{\mathrm{Tr}[\mathcal{M}_{\alpha,11}\mathcal{M}_{\beta,11}]}_{\mathcal{O}(1)} + \underbrace{\mathrm{Tr}[\mathcal{M}_{\alpha,12}\mathcal{M}_{\beta,21}]}_{\mathcal{O}(1/\sigma_S^2)} + \underbrace{\mathrm{Tr}[\mathcal{M}_{\alpha,21}\mathcal{M}_{\beta,12}]}_{\mathcal{O}(1/\sigma_S^2)} + \underbrace{\mathrm{Tr}[\mathcal{M}_{\alpha,22}\mathcal{M}_{\beta,22}]}_{\mathcal{O}(1/\sigma_S^4)}\Big\}. \tag{3.39}$$

In the above equation, the term in the right-hand side of the first line denotes the upper left $N \times N$ block of $\mathcal{M}_\alpha\mathcal{M}_\beta$, and the term in the second line denotes the lower right $M \times M$ block (with N and M controlling, respectively, the pulsar and star numbers). We explicitly indicate the order of the expansion in the small $1/\sigma_S^2$ parameter.

In fact, working in a noise-dominated, large σ_S regime for astrometry, we write—up to first order in σ_S^{-2},

$$\mathcal{M}_\alpha = \mathcal{M}_\alpha^{(0)} + \sigma_S^{-2}\mathcal{M}_\alpha^{(1)}, \tag{3.40}$$

with

$$\mathcal{M}_\alpha^{(0)} = \begin{bmatrix} A_\alpha A^{-1} & 0 \\ B_\alpha^T A^{-1} & 0 \end{bmatrix}, \tag{3.41}$$

$$\mathcal{M}_\alpha^{(1)} = \begin{bmatrix} A_\alpha A^{-1} BB^T A^{-1} - B_\alpha B^T A^{-1} & B_\alpha - A_\alpha A^{-1} B \\ B_\alpha^T A^{-1} BB^T A^{-1} - D_\alpha B^T A^{-1} & D_\alpha - B_\alpha^T A^{-1} B \end{bmatrix}. \tag{3.42}$$

Explicitly, an expansion of the Fisher matrix up to order $1/\sigma_S^2$ gives the formula

$$\mathcal{F}_{\alpha\beta} = \frac{1}{2}\mathrm{Tr}[\mathcal{M}_\alpha^{(0)}\mathcal{M}_\beta^{(0)}] + \frac{1}{2\sigma_S^2}\mathrm{Tr}[\mathcal{M}_\alpha^{(0)}\mathcal{M}_\beta^{(1)} + \mathcal{M}_\alpha^{(1)}\mathcal{M}_\beta^{(0)}] \tag{3.43}$$

$$= \frac{1}{2}\mathrm{Tr}[A_\alpha A^{-1} A_\beta A^{-1}] + \frac{1}{2\sigma_S^2}\mathrm{Tr}[A_\alpha A^{-1} A_\beta A^{-1} BB^T A^{-1} - A_\alpha A^{-1} B_\beta B^T A^{-1} - A_\alpha A^{-1} BB_\beta^T A^{-1}] + \frac{1}{2\sigma_S^2}\mathrm{Tr}[A_\alpha A^{-1} BB^T A^{-1} A_\beta A^{-1} - B_\alpha B^T A^{-1} A_\beta A^{-1} - B_\alpha^T A^{-1} A_\beta A^{-1} B] + \frac{1}{2\sigma_S^2}\mathrm{Tr}[B_\alpha^T A^{-1} B_\beta + B_\alpha B_\beta^T A^{-1}]. \tag{3.44}$$

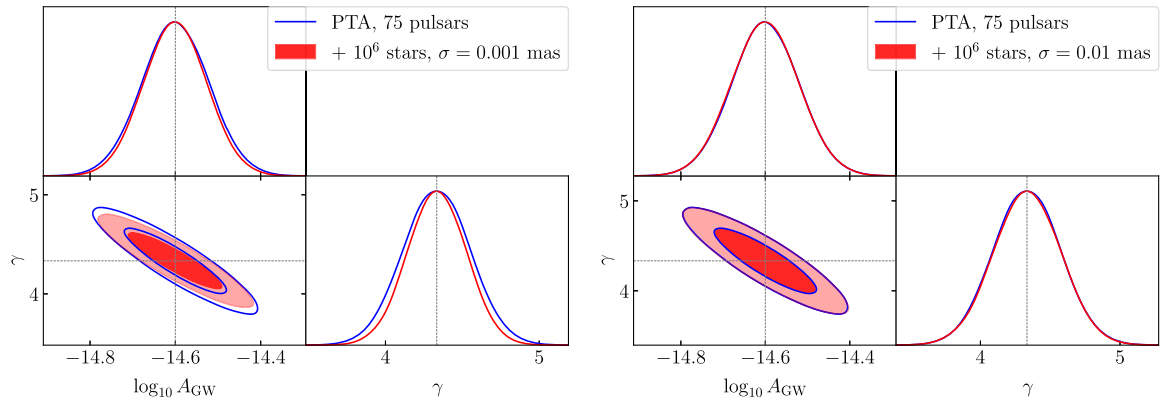

FIG. 8. Fisher forecast for the amplitude and slope of the SGWB for a fiducial value $\log_{10} A_{\rm GW} = -14.6, \gamma = 13/3$. Red indicates the PTA-only case with the number of pulsars and noise parameters chosen to match the sensitivity of the combined IPTA dataset [9]. Blue shows the forecasts for the addition of PTA-astrometry cross-correlations with 10^6 stars. Left panel: astrometry noise $\sigma = 0.001$ mas. Right panel: astrometry noise $\sigma = 0.01$ mas.

At zeroth order in $1/\sigma_S^2$, we recover the PTA-only Fisher matrix—first line of Eq. (3.44). At order $\mathcal{O}(1/\sigma_S^2)$, we obtain the first corrections to the PTA-only forecasts, associated with synergies with astrometry. Since the relevant terms always include the matrix B, such corrections include the pulsar-star correlations. Notice that this perturbative expansion of the Fisher matrix greatly simplifies the numerical calculations in the astrometric noise-dominated regime since we only have to deal with matrices of size $N \times N$ and $N \times M$ but not $M \times M$ where M can be of the order 10^5 or larger. (Recall that N is the number of pulsars, and M is twice the number of stars which are monitored.) On the other hand, for typical pulsar datasets, currently and in the near future, we have to handle matrices of size $N \sim \mathcal{O}(100)$, which is manageable with standard computing resources.

We now use this approach to compute the full Fisher matrix, combining the individual per-frequency Fisher matrices. In Fig. 8, we present our results for a PTA setup with 75 pulsars and an astrometric setup with 10^6 stars. The astrometric setup has $\Delta\theta_{\rm rms} = 0.01, 0.001$ mas and $T_{\rm cad} = {\rm year}/15$, i.e., roughly corresponding to the observational cadence of Gaia. Our results indicate that, for the case with $\sigma = 0.001$ mas, we obtain a roughly $\mathcal{O}(10\%)$ improvement over the PTA-only constraints, while for $\sigma \geq 0.01$ mas, the improvement will be negligible.[14] See Table I for the exact numbers.

[14]We note that for the $\sigma = 0.001$ mas case, the weak-signal limit does not hold for the first few frequency bins where the signal and noise are comparable in magnitude. However, we have checked (with a lower number of stars) that for similar noise vs signal strengths, the results from the series expansion match fairly well with the full numerical results.

3. Case of dipolar anisotropy

We conclude our analysis with a discussion of the prospects to detect a possible SGWB dipolar anisotropy through the synergy of astrometry and PTA. We aim to quantify the minimal level of anisotropy detectable by perspective PTA-only data and with the joint system astrometry-PTA using the same configurations as in the previous section. Although our analysis is tailored to the kinematic dipole [see Eq. (2.8)], we expect that similar considerations hold for the case of dipolar statistical anisotropies, of which the kinematic dipole is just a specific case. Given the crucial role that anisotropies may play in distinguishing astrophysical versus cosmological sources of SGWB, such a question is important to address. Notice that current upper limits on the magnitude of SGWB anisotropies lie at the 10% level relative to the monopole [66,102].

We carry out the analysis with the same approach developed in Sec. III B. The components A, B, D entering in the covariance matrix (3.23) now read

$$A_{pq} = \frac{(\gamma_{pq}^{(0)} + \gamma_{pq}^{(1)}) I_f}{(4\pi f)^2} + \sigma_p^2 \delta_{pq}, \tag{3.45}$$

TABLE I. Fiducial parameter values and marginalized 1σ limits from the Fisher forecast. We focus on synergy measurements of the SGWB monopole as discussed in Sec. III B 2.

	$\log A_{\rm GW}$	γ
PTA only	-14.6 ± 0.079	$13/3 \pm 0.24$
PTA + Astrometry, $\sigma = 0.001$ mas	-14.6 ± 0.072	$13/3 \pm 0.19$
PTA + Astrometry, $\sigma = 0.01$ mas	-14.6 ± 0.079	$13/3 \pm 0.24$

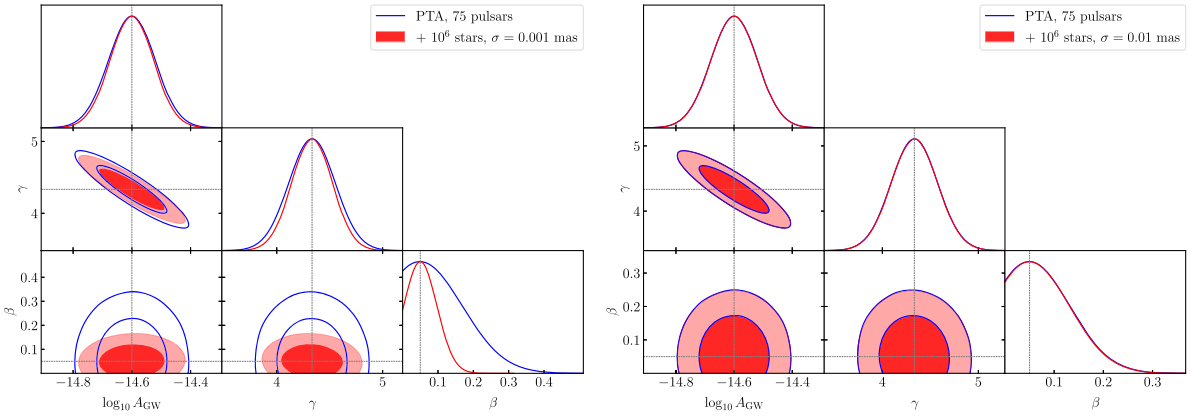

FIG. 9. Fisher forecast for the SGWB parameters, with the addition of the dipole.

$$B_{pa} = \frac{(K^{(0)}_{p,a} + K^{(1)}_{p,a}) I_f}{(4\pi)^2 f}, \tag{3.46}$$

$$D_{ab} = \frac{(H^{(0)}_{ab} + H^{(1)}_{ab})}{4\pi} I_f + \delta_{ab}\sigma_a^2. \tag{3.47}$$

Besides the monopole, we now include the contributions to the dipole ORF: $\gamma^{(1)}$ for PTA [71], $K^{(1)}$ for the cross-correlation and astrometry-only $H^{(1)}$ (see Sec. II). The analysis proceeds in the same manner as the previous section, and the results are plotted in Fig. 9. The fiducial parameter means and the marginalized 1σ Fisher errors are collected in Table II.

We choose the same fiducial $A_{\rm GW}$ and γ as in Sec. III B 1. We select a level of dipole anisotropy $\beta = 5 \times 10^{-2}$, finding this value to be the minimum level of kinematic dipole that will detectable with our PTA + Astrometry setup. Thus, astrometry can again help to tighten the constraints on the dipole anisotropy, which can be useful in determining the origin of the SGWB. Given that the sensitivity to the SGWB is likely to be dominated by PTA datasets even in the near future, one would likely require futuristic PTA experiments combined with futuristic astrometric surveys to reach the CMB kinematic dipole level. Reaching the CMB kinematic dipole level ($\beta = 1.23 \times 10^{-3}$) with PTA alone requires a substantial increase in the number of pulsars ($N > 1000$) [88,102] which may only be achievable with SKA. It would also be interesting to explore how cross-correlations with astrometric datasets could work to improve SGWB sensitivity in the SKA era.

IV. CONCLUSIONS

In the next few years, evidence for the SGWB in the nHz range is likely to grow as PTA experiments collect more and more data. We can expect an increased statistical significance for the Hellings-Downs correlation, as well as tighter constraints on the amplitude and frequency spectrum of the SGWB. The next generation of radio telescopes, SKA, is expected to begin operations in the early 2030s and is projected to observe a large number of pulsars with unprecedented timing precision [15], possibly leading to a precise determination of the SGWB parameters. A complementary probe of the nHz SGWB is provided by astrometry—corresponding to the precise monitoring of the positions of a large number of stars. Data from astrometric surveys such as Gaia have already been used to constrain SGWB in the frequency range $f \lesssim 10^{-9}$ Hz [40–43]. In this work, we have considered how astrometry data in the nHz band will complement PTA observations and how it can be used to characterize the properties of SGWB beyond what can be obtained from PTA-only data.

In Sec. II, we first reviewed the theory behind the astrometric detection of SGWB and derived, for the first time, fully covariant, analytical expressions for the kinematic dipole ORFs of the autocorrelation of the astrometric deflections, as well as their cross-correlation with pulsar timing residuals. Our expressions allowed us to

TABLE II. Fiducial parameter values and marginalized 1σ limits from the Fisher forecast. In this table, we report limits on the size of the dipolar anisotropy, as discussed in Sec. III B 3.

	$\log A_{\rm GW}$	γ	β
PTA only	-14.6 ± 0.079	$13/3 \pm 0.24$	0.05 ± 0.081
PTA + Astrometry, $\sigma = 0.001$ mas	-14.6 ± 0.072	$13/3 \pm 0.18$	0.05 ± 0.048
PTA + Astrometry, $\sigma = 0.01$ mas	-14.6 ± 0.079	$13/3 \pm 0.24$	0.05 ± 0.080

manifestly visualize the sensitivity of the astrometric and PTA setups to the SGWB properties, as a function of the locations of monitored objects.

In Sec. III, we studied the sensitivity of the astrometric and PTA setups to the SGWB, focusing on the measurement of the SGWB amplitude, the spectral tilt, and the magnitude of the kinematic dipole anisotropy. In Appendix C, we derived optimal estimators for SGWB monopole and dipole measurements in this context, built in terms of quadratic combinations of the astrometric deflections. We used these formulas to forecast the sensitivity of astrometry to the SGWB monopole and dipole, assuming a large number of stars uniformly distributed across the sky. In Sec. III B, we analyzed the joint PTA-astrometry setup and showed that cross-correlating PTA and astrometry data could tighten the constraints on SGWB obtained from PTA data alone. We used Fisher forecasts to calculate the sensitivity to the SGWB amplitude, spectral shape, and dipole, finding that an astrometric survey with 0.01 mas astrometric precision and the typical number of sources and cadence of Gaia could lead to noticeable improvements over current PTA-only SGWB constraints. Improvements on the PTA constraints can be quite useful since tighter constraints on the SGWB parameters can be used to rule out models and potentially distinguish between astrophysical and cosmological signals. Reaching the level of sensitivity required to detect the CMB level kinematic dipole anisotropy in the SGWB is likely to require both futuristic PTA experiments such as SKA and futuristic astrometric surveys.

The flood of upcoming data from PTA and astrometry experiments present both challenges and opportunities. The possibility of a joint PTA-astrometry data analysis holds exciting potential since cross-correlations between timing residuals and astrometric deflections could be leveraged to deliver tighter SGWB constraints compared to either of the experiments alone. Thus, developing efficient implementations of joint PTA-astrometry analysis will be crucial for harnessing the power of these cross-correlations. It would also be interesting to further explore such synergies in the context of general SGWB anisotropies and study their detectability. We leave such pursuits to future work.

ACKNOWLEDGMENTS

This work was partially funded by the STFC Grants No. ST/T000813/1 and No. ST/X000648/1. We also acknowledge the support of the Supercomputing Wales project, which is partly funded by the European Regional Development Fund (ERDF) via the Welsh Government. We acknowledge the use of the GetDist software package for visualizing the results of the Fisher forecasts [107]. The codes used to perform the numerical calculations and plot the results in this paper are publicly available on GitHub. For the purpose of open access, the authors have applied a Creative Commons Attribution licence to any author accepted manuscript version arising.

DATA AVAILABILITY

The data that support the findings of this article are openly available [1].

APPENDIX A: SPECTRUM OF ANGULAR DEFLECTION FLUCTUATIONS

In this appendix, we make use of our analytical, covariant expressions for the ORF to show that dipolar anisotropies induce correlations between electric and magnetic components of star deflections. We use the notation of [25], to which we refer the reader for more details on the nomenclature.

The EB correlation will be given by

$$C_{ElmBl'm'} = \frac{1}{\ell(\ell+1)} \int d^2\Omega_n d^2\Omega_{n'} Y^*_{lm}(n) Y_{l'm'}(n') \beta(4-n_\Omega) \beta^{EB}, \tag{A1}$$

where

$$\beta^{EB} = \nabla_i \nabla'_b [\epsilon_{jab} n_a H^{(1)}_{ij}]. \tag{A2}$$

Here, ∇_i and ∇'_b are normal 3D derivatives with respect to $\mathbf{z}$ and $\mathbf{z}'$ with $\mathbf{n} = \mathbf{z}/|\mathbf{z}|$, $\mathbf{q} = \mathbf{z}'/|\mathbf{z}'|$. Now, we only need to focus on the parts of $H^{(1)}_{ij}$ [see (2.17)] that are not invariant under $\mathbf{n} \to -\mathbf{n}$ and $\mathbf{q} \to -\mathbf{q}$, as these give a zero contribution [25]. Thus, we only have the following contribution:

$$\begin{aligned} \beta^{EB} &= \nabla_i \nabla'_b [a_1 \epsilon_{jab} n_a (\epsilon^{ilm} n_l q_m [(\mathbf{n}\cdot\mathbf{q}) q^j - n^j] + \epsilon^{jlm} n_l q_m [(\mathbf{n}\cdot\mathbf{q}) n^i - q^i])] \\ &= \nabla_i \nabla'_b [a_1 T^{bi}], \end{aligned} \tag{A3}$$

where

$$T^{bi} = (q^b - (\mathbf{n}\cdot\mathbf{q})n^b)(q^i + n^i)((\mathbf{n}\cdot\mathbf{q}) - 1) - (n^i q^b - (\mathbf{n}\cdot\mathbf{q})\delta^{ib})((\mathbf{n}\cdot\mathbf{q})^2 - 1), \tag{A4}$$

and a_1 is defined in (2.19). Thus, we need $\nabla_i X, \nabla'_b X, \nabla_i \nabla'_b X$, where $X = a_1, T^{bi}$. We can use the relations $\nabla_i n_j = \delta_{ij} - n_i n_j$, $\nabla'_i q_j = \delta_{ij} - q_i q_j$, $\nabla_i q_j = \nabla'_i n_j = \nabla_i v_j = \nabla'_i v_j = 0$, as well as

$$\nabla_i(\mathbf{n}\cdot\mathbf{q}) = q_i - (\mathbf{n}\cdot\mathbf{q})n_i, \qquad \nabla'_b(\mathbf{n}\cdot\mathbf{q}) = n_b - (\mathbf{n}\cdot\mathbf{q})q_b. \tag{A5}$$

Using these, we find

$$\nabla_i\nabla'_b(a_1)T^{bi} = -\frac{\pi}{12}\varepsilon^{ljk}v_l n_j q_k F_1\left[2 - \left(-3 + \frac{F_{1,y}}{F_1}(\mathbf{n}\cdot\mathbf{q} - 1) - 2\mathbf{n}\cdot\mathbf{q}\right)(\mathbf{n}\cdot\mathbf{q})^2(\mathbf{n}\cdot\mathbf{q} - 1)\right], \tag{A6a}$$

$$\nabla_i(a_1)\nabla'_b(T^{bi}) = -\frac{\pi}{12}\varepsilon^{ljk}v_l n_j q_k F_1(1 - \mathbf{n}\cdot\mathbf{q})[-1 + (\mathbf{n}\cdot\mathbf{q})^2(\mathbf{n}\cdot\mathbf{q}(\mathbf{n}\cdot\mathbf{q} - 7) - 1)], \tag{A6b}$$

$$\nabla'_b(a_1)\nabla_i(T^{bi}) = -\frac{\pi}{6}\varepsilon^{ljk}v_l n_j q_k(1 + \mathbf{n}\cdot\mathbf{q} + (\mathbf{n}\cdot\mathbf{q})^2(2 + \mathbf{n}\cdot\mathbf{q}))\left(F_2\mathbf{n}\cdot\mathbf{q} + \frac{F_1}{2}(1 - (\mathbf{n}\cdot\mathbf{q})^2)\right), \tag{A6c}$$

$$(a_1)\nabla_i\nabla'_b(T^{bi}) = \frac{\pi}{6}\varepsilon^{ljk}v_l n_j q_k F_2[1 - \mathbf{n}\cdot\mathbf{q}(2 + \mathbf{n}\cdot\mathbf{q}[4 + \mathbf{n}\cdot\mathbf{q}(3\mathbf{n}\cdot\mathbf{q} - 10)])], \tag{A6d}$$

where we defined

$$F_1 = \frac{(-1 + 4y - 14y^2 + 11y^3 - 3y^2(2y + 1)\ln(y))}{(y^2(1 - y)^4)}, \tag{A7}$$

$$F_2 = \frac{\left(1 - 4y - \frac{3y^2\ln(y)}{(1-y)}\right)}{y(1 - y)^2}, \tag{A8}$$

to simplify notation, and $F_{1,y} = dF_1/dy$. Combining and simplifying these, we get for (A3)

$$\beta^{EB} = \frac{\pi}{12}\mathbf{v}\cdot(\mathbf{n}\times\mathbf{q})G(y), \tag{A9}$$

where

$$\begin{aligned} G(y) = -\frac{2}{y^2(y-1)^5}[&(y-1)(-1 + 6y - 42y^2 + 170y^3 - 481y^4 + 800y^5 - 684y^6 + 208y^7 + 96y^8) \\ &- 3y^2(-1 - y + 13y^2 - 77y^3 + 198y^4 - 236y^5 + 128y^6)\ln(y)], \end{aligned} \tag{A10}$$

where y is defined in Eq. (2.14). Note that β^{EB} depends on the angles that $\mathbf{v}$ makes with $\mathbf{n}$ and $\mathbf{q}$, as well as on ζ.

APPENDIX B: ANGULAR DEPENDENCE OF OVERLAP REDUCTION FUNCTIONS

In this appendix, we report explicit formulas for the traces of matrix combinations used in Sec. II for representing the sensitivity of the PTA and astrometry system to the properties of SGWB. From Eqs. (2.15) and (2.26), we find

$$\mathrm{Tr}[\boldsymbol{H}_0\boldsymbol{H}_0] = \frac{\pi^2(\cos^2(\zeta) + 1)}{9(\cos(\zeta) + 1)^2}\left(-7\cos^2(\zeta) - 2\cos(\zeta) + 6(\cos(\zeta) - 1)^2\ln\left(\sin^2\left(\frac{\zeta}{2}\right)\right) + 5\right)^2; \tag{B1}$$

$$\mathbf{K}_0\mathbf{K}_0^T = \frac{16}{9}\pi^2\tan^2\left(\frac{\zeta_{sp}}{2}\right)\left(-3\ln(1 - \cos(\zeta_{sp})) + \cos(\zeta_{sp})\left(3\ln\left(\sin^2\left(\frac{\zeta_{sp}}{2}\right)\right) - 2\right) - 2 + \ln(8)\right)^2, \tag{B2}$$

where ζ is the angle between the stars at directions $\mathbf{n}$ and $\mathbf{q}$, while ζ_{sp} is the angle between a star in direction $\mathbf{n}$ and a pulsar at direction $\mathbf{x}$.

With Eqs. (2.17) and (2.29), we get

$$\mathrm{Tr}[\boldsymbol{H}_1\boldsymbol{H}_1] = \frac{64\pi^2(\alpha_H(Av)^2\sqrt{1-y}y^2 + 4\delta_H^2(y-1)y^4(\beta_H - \gamma_H\sqrt{1-y}))}{9((nq)^2-1)^2(1-y)^{5/2}}; \tag{B3}$$

$$\mathbf{K}_1\mathbf{K}_1^T = \frac{4\pi^2(nx^2-1)((nx+1)^2(\alpha_K\beta_K^2 - (A_1v)^4(5-6nx)^2) + 12\gamma_K\ln(\frac{1-nx}{2}))}{9(nx+1)^4((A_1v)-(A_1v)nx)^2}, \tag{B4}$$

where

$$\alpha_H = -(y-1)^2(nq^2y^2(2y+1)^2 + 2nq(1-4y)^2 + y^2(2y+1)^2) + 6(y-1)y^2(2(nq^2+1)y^2 + nq(nq+8)y - 2nq + y)\ln(y) - 9(nq+1)^2y^4\ln^2(y), \tag{B5}$$

$$\beta_H = (nq)^2(nv)(y-1)\sqrt{\frac{(Av)^2}{y-1} + 4((nv)^2-1)y} - (nv)\sqrt{1-y}\sqrt{4((nv)^2-1)(y-1)y - (Av)^2}, \tag{B6}$$

$$\gamma_H = (nv)^2((nq)^2 - 2y + 1) + (nq)^2(-y) + y, \tag{B7}$$

$$\delta_H = 1 + y - 2y^2 + 3y\ln y, \tag{B8}$$

and

$$\alpha_K = -1 + (nv)^2 + (nx)^2 - 2nv(nx)(vx) + (vx)^2, \tag{B9}$$

$$\beta_K = nv(4 + nx(-7+2nx)) + (4 + 3(-2+nx)nx)vx, \tag{B10}$$

$$\gamma_K = (-1+nx)^2(1+nx)((A_1v)^4(-5+6nx) + (nv+vx)\alpha_K\beta_K) + 3(-1+nx)^4(-(A_1v)^4 + (nv+vx)^2\alpha_K)\ln\left(\frac{1-nx}{2}\right). \tag{B11}$$

When the vector $\mathbf{n}$ is parallel to $\mathbf{v}$, then $Av = 0$, and Eq. (B3) is simpler. For this case, $\mathbf{K}_1\mathbf{K}_1^T$ is calculated with (2.30). More specifically, when $\mathbf{n} = -\mathbf{v}$, we get

$$\mathrm{Tr}[\boldsymbol{H}_1\boldsymbol{H}_1] = \frac{4\pi^2(\cos(\zeta)-1)^2(\cos^2(\zeta)+1)}{9(\cos(\zeta)+1)^2}(\cos^2(\zeta) - \cos(\zeta) - \ln(8)\cos(\zeta) + 3(\cos(\zeta)-1)\ln(1-\cos(\zeta)) - 2 + \ln(8))^2, \tag{B12}$$

$$\mathbf{K}_1\mathbf{K}_1^T = \frac{1}{9}\pi^2\tan^2\left(\frac{\zeta_{sp}}{2}\right)\left(2\cos(\zeta_{sp}) - 3\cos(2\zeta_{sp}) - 12(\cos(\zeta_{sp})-1)\ln\left(\sin^2\left(\frac{\zeta_{sp}}{2}\right)\right) + 5\right)^2. \tag{B13}$$

Similar expressions are obtained for the case $\mathbf{n} = \mathbf{v}$.

APPENDIX C: OPTIMAL ESTIMATORS

In this appendix, we briefly discuss how to build optimal estimators for the coefficients p_n formally appearing in the sum (3.1), later specializing to the monopole and dipole cases with p_0 and p_1. The determination of these coefficients allows us to infer the properties of the SGWB. First, we recall here that we can expand the astrometric deflection correlation in terms of these basis coefficients p_n as

$$\langle \delta n_a^i \delta n_b^j \rangle \equiv C_{ab}^{ij} = \sum_n p_n H_{ab,n}^{ij} + N_{ab}^{ij}, \tag{C1}$$

in terms of the response H and the noise N. Now, following the approach previously developed for the CMB [108], a quadratic estimator for p_n can be formally expressed as

$$\hat{p}_n = \delta n_a^i E_{ab,n}^{ij} \delta n_b^j - b_n, \tag{C2}$$

in terms of a symmetric matrix $E_{ab,n}$ and a vector b_n.

We wish to determine the corresponding values of these quantities which render the estimator unbiased, i.e., $\langle \hat{p}_n \rangle = p_n$, and minimize its variance. Taking the expectation value of the estimator, we find

$$\langle \hat{p}_n \rangle = \sum_{n'} W_{nn'} p_{n'} + \mathrm{Tr}[\boldsymbol{E}_n \boldsymbol{N}] - b_n, \quad \text{with}$$
$$W_{nn'} \equiv \mathrm{Tr}[\boldsymbol{H}_{n'} \boldsymbol{E}_n]. \tag{C3}$$

Thus, the quantity b_n should be chosen as $b_n = \mathrm{Tr}[\boldsymbol{E}_n \boldsymbol{N}]$ to ensure that the estimator is unbiased. The covariance of the matrix of the estimators $\mathrm{Cov}(\hat{p}_n, \hat{p}_{n'}) \equiv \langle (\hat{p}_n - \langle \hat{p}_n \rangle)(\hat{p}_{n'} - \langle \hat{p}_{n'} \rangle) \rangle$, assuming that the astrometric deflections obey a Gaussian distribution, can be written as

$$\mathrm{Cov}(\hat{p}_n, \hat{p}_{n'}) = [C^{il}_{ad} C^{jk}_{bc} + C^{ik}_{ac} C^{kl}_{bd}] E^{ij}_{ab,n} E^{kl}_{cd,n'} \tag{C4}$$
$$= 2\mathrm{Tr}[\boldsymbol{C}\boldsymbol{E}_n \boldsymbol{C}\boldsymbol{E}_{n'}]. \tag{C5}$$

The solution for the matrix $\boldsymbol{E}_n$ which minimizes this variance under the normalization constraint $W_{nn} = 1$ is given by [108]

$$\boldsymbol{E}_n = \frac{\boldsymbol{C}^{-1} \boldsymbol{H}_n \boldsymbol{C}^{-1}}{\mathrm{Tr}[\boldsymbol{C}^{-1} \boldsymbol{H}_n \boldsymbol{C}^{-1} \boldsymbol{H}_n]}, \tag{C6}$$

so that

$$W_{nn'} = \frac{\mathrm{Tr}[\boldsymbol{C}^{-1} \boldsymbol{H}_{n'} \boldsymbol{C}^{-1} \boldsymbol{H}_n]}{\mathrm{Tr}[\boldsymbol{C}^{-1} \boldsymbol{H}_n \boldsymbol{C}^{-1} \boldsymbol{H}_n]}. \tag{C7}$$

The variance of the individual $\hat{p}_n$ is thus

$$\mathrm{Var}(\hat{p}_n) = \frac{2}{\mathrm{Tr}[\boldsymbol{C}^{-1} \boldsymbol{H}_n \boldsymbol{C}^{-1} \boldsymbol{H}_n]}. \tag{C8}$$

This estimator is optimal in the sense that it is unbiased and that its variance is equal to what we obtained using the Fisher matrix approach in Sec. III A, making it the minimal variance estimator that saturates the Cramer-Rao bound (see [99,108] for a detailed discussion).

The expressions obtained here are completely general and valid for arbitrary distributions of stars with arbitrary noise properties which are encoded in the noise matrix $\boldsymbol{N}$. Further simplifications can be made in the noise-dominated limit with the diagonal noise where the solution reduces to

$$\boldsymbol{E}_n = \frac{\boldsymbol{H}_n}{\mathrm{Tr}[\boldsymbol{H}_n \boldsymbol{H}_n]}, \qquad W_{nn'} = \frac{\mathrm{Tr}[\boldsymbol{H}_n \boldsymbol{H}_{n'}]}{\mathrm{Tr}[\boldsymbol{H}_n \boldsymbol{H}_n]}. \tag{C9}$$

Finally, in the special case where one only wishes to estimate a single p_n, e.g., the monopole, from the data, the estimators become trivial,

$$\hat{p}_n = \frac{\delta n^i_a H^{ij}_{ab,n} \delta n^j_b}{(\mathrm{Tr}[\boldsymbol{H}_n \boldsymbol{H}_n])} - b_n. \tag{C10}$$

[1] Z. Arzoumanian *et al.* (NANOGrav Collaboration), The NANOGrav 12.5 yr data set: Search for an isotropic stochastic gravitational-wave background, Astrophys. J. Lett. **905**, L34 (2020).

[2] B. Goncharov *et al.*, On the evidence for a common-spectrum process in the search for the nanohertz gravitational-wave background with the parkes pulsar timing array, Astrophys. J. Lett. **917**, L19 (2021).

[3] S. Chen *et al.* (EPTA Collaboration), Common-red-signal analysis with 24-yr high-precision timing of the European pulsar timing array: Inferences in the stochastic gravitational-wave background search, Mon. Not. R. Astron. Soc. **508**, 4970 (2021).

[4] J. Antoniadis *et al.*, The international pulsar timing array second data release: Search for an isotropic gravitational wave background, Mon. Not. R. Astron. Soc. **510**, 4873 (2022).

[5] G. Agazie *et al.* (NANOGrav Collaboration), The NANOGrav 15 yr data set: Evidence for a gravitational-wave background, Astrophys. J. Lett. **951**, L8 (2023).

[6] J. Antoniadis *et al.* (EPTA and InPTA Collaborations), The second data release from the European Pulsar Timing Array—III. Search for gravitational wave signals, Astron. Astrophys. **678**, A50 (2023).

[7] D. J. Reardon *et al.*, Search for an isotropic gravitational-wave background with the parkes pulsar timing array, Astrophys. J. Lett. **951**, L6 (2023).

[8] H. Xu *et al.*, Searching for the nano-hertz stochastic gravitational wave background with the Chinese pulsar timing array data release I, Res. Astron. Astrophys. **23**, 075024 (2023).

[9] G. Agazie *et al.* (International Pulsar Timing Array Collaboration), Comparing recent PTA results on the nanohertz stochastic gravitational wave background, arXiv:2309.00693.

[10] M. T. Miles *et al.*, The MeerKAT pulsar timing array: The first search for gravitational waves with the MeerKAT radio telescope, arXiv:2412.01153.

[11] R. W. Hellings and G. S. Downs, Upper limits on the isotopic gravitational radiation background from pulsar timing analysis, Astrophys. J. Lett. **265**, L39 (1983).

[12] A. Sesana, A. Vecchio, and C. N. Colacino, The stochastic gravitational-wave background from massive black hole binary systems: Implications for observations with Pulsar

Timing Arrays, Mon. Not. R. Astron. Soc. **390**, 192 (2008).
[13] S. Burke-Spolaor *et al.*, The astrophysics of nanohertz gravitational waves, Astron. Astrophys. Rev. **27**, 5 (2019).
[14] C. Caprini and D. G. Figueroa, Cosmological backgrounds of gravitational waves, Classical Quantum Gravity **35**, 163001 (2018).
[15] G. Janssen *et al.*, Gravitational wave astronomy with the SKA, Proc. Sci., AASKA14 (**2015**) 037 [arXiv:1501.00127].
[16] E. F. Keane *et al.*, A cosmic census of radio pulsars with the SKA, Proc. Sci., AASKA14 (**2015**) 040 [arXiv:1501.00056].
[17] E. V. Linder, Relativistic scattering coherence, Phys. Rev. D **34**, 1759 (1986).
[18] V. B. Braginsky, N. S. Kardashev, I. D. Novikov, and A. G. Polnarev, Propagation of electromagnetic radiation in a random field of gravitational waves and space radio interferometry, Nuovo Cimento Soc. Ital. Fis. **105B**, 1141 (1990).
[19] R. Fakir, Gravity wave watching, Astrophys. J. **426**, 74 (1994).
[20] T. Pyne, C. R. Gwinn, M. Birkinshaw, T. M. Eubanks, and D. N. Matsakis, Gravitational radiation and very long baseline interferometry, Astrophys. J. **465**, 566 (1996).
[21] N. Kaiser and A. H. Jaffe, Bending of light by gravity waves, Astrophys. J. **484**, 545 (1997).
[22] C. R. Gwinn, T. M. Eubanks, T. Pyne, M. Birkinshaw, and D. N. Matsakis, Quasar proper motions and low frequency gravitational waves, Astrophys. J. **485**, 87 (1997).
[23] S. M. Kopeikin, G. Schaefer, C. R. Gwinn, and T. M. Eubanks, Astrometric and timing effects of gravitational waves from localized sources, Phys. Rev. D **59**, 084023 (1999).
[24] B. F. Schutz, Astrometric and timing effects of gravitational waves, Proc. Int. Astron. Union **5**, 234 (2009).
[25] L. G. Book and E. E. Flanagan, Astrometric effects of a stochastic gravitational wave background, Phys. Rev. D **83**, 024024 (2011).
[26] C. J. Moore, D. P. Mihaylov, A. Lasenby, and G. Gilmore, Astrometric search method for individually resolvable gravitational wave sources with gaia, Phys. Rev. Lett. **119**, 261102 (2017).
[27] S. A. Klioner, Gaia-like astrometry and gravitational waves, Classical Quantum Gravity **35**, 045005 (2018).
[28] D. P. Mihaylov, C. J. Moore, J. R. Gair, A. Lasenby, and G. Gilmore, Astrometric effects of gravitational wave backgrounds with non-Einsteinian polarizations, Phys. Rev. D **97**, 124058 (2018).
[29] W. Qin, K. K. Boddy, M. Kamionkowski, and L. Dai, Pulsar-timing arrays, astrometry, and gravitational waves, Phys. Rev. D **99**, 063002 (2019).
[30] G. Mentasti and C. R. Contaldi, Observing gravitational waves with solar system astrometry, J. Cosmol. Astropart. Phys. 05 (2024) 028.
[31] K. Inomata, M. Kamionkowski, C. M. Toral, and S. R. Taylor, Overlap reduction functions for pulsar timing arrays and astrometry, Phys. Rev. D **110**, 063547 (2024).
[32] H. An, T. Li, J. Shu, X. Wang, X. Xue, and Y. Zhao, Dark photon dark matter and low-frequency gravitational wave detection with gaia-like astrometry, arXiv:2407.16488.
[33] A. H. Jaffe, Observing gravitational radiation with QSO proper motions and the SKA, New Astron. Rev. **48**, 1483 (2004).
[34] Z. Lu, L.-T. Wang, and H. Xiao, A new probe of μHz gravitational waves with FRB timing, arXiv:2407.12920.
[35] L. Zwick, D. Soyuer, D. J. D'Orazio, D. O'Neill, A. Derdzinski, P. Saha, D. Blas, A. C. Jenkins, and L. Z. Kelley, Bridging the micro-Hz gravitational wave gap via Doppler tracking with the Uranus Orbiter and Probe Mission: Massive black hole binaries, early universe signals and ultra-light dark matter, arXiv:2406.02306.
[36] T. Prusti *et al.* (Gaia Collaboration), The gaia mission, Astron. Astrophys. **595**, A1 (2016).
[37] A. Vallenari, A. G. A. Brown *et al.*, Gaia data release 3: Summary of the content and survey properties, Astron. Astrophys. **674**, A1 (2023).
[38] W. Schlüter and D. Behrend, The international VLBI service for geodesy and astrometry (IVS): Current capabilities and future prospects, J. Geodes. **81**, 379 (2007).
[39] O. Titov, S. B. Lambert, and A.-M. Gontier, VLBI measurement of the secular aberration drift, Astron. Astrophys. **529**, A91 (2011).
[40] J. Darling, A. E. Truebenbach, and J. Paine, Astrometric limits on the stochastic gravitational wave background, Astrophys. J. **861**, 113 (2018).
[41] S. Aoyama, D. Yamauchi, M. Shiraishi, and M. Ouchi, Gaia 400,894 QSO constraint on the energy density of low-frequency gravitational waves, arXiv:2105.04039.
[42] S. Jaraba, J. García-Bellido, S. Kuroyanagi, S. Ferraiuolo, and M. Braglia, Stochastic gravitational wave background constraints from Gaia DR3 astrometry, Mon. Not. R. Astron. Soc. **524**, 3609 (2023).
[43] J. Darling, A new approach to the low frequency stochastic gravitational wave background: Constraints from quasars and the astrometric hellings-downs curve, arXiv:2412.08605.
[44] R. E. Sanderson, A. Bellini *et al.*, Astrometry with the wide-field infrared space telescope, arXiv:1712.05420.
[45] Y. Wang, K. Pardo, T.-C. Chang, and O. Doré, Gravitational wave detection with photometric surveys, Phys. Rev. D **103**, 084007 (2021).
[46] Y. Wang, K. Pardo, T.-C. Chang, and O. Doré, Constraining the stochastic gravitational wave background with photometric surveys, Phys. Rev. D **106**, 084006 (2022).
[47] K. Pardo, T.-C. Chang, O. Doré, and Y. Wang, Gravitational wave detection with relative astrometry using Roman's galactic bulge time domain survey, arXiv:2306.14968.
[48] C. Boehm *et al.* (Theia Collaboration), Theia: Faint objects in motion or the new astrometry frontier, arXiv:1707.01348.
[49] F. Malbet *et al.*, Theia: Science cases and mission profiles for high precision astrometry in the future, in *SPIE Astronomical Telescopes+Instrumentation 2022* (SPIE, 2022). arXiv:2207.12540.

[50] J. Garcia-Bellido, H. Murayama, and G. White, Exploring the early Universe with Gaia and Theia, J. Cosmol. Astropart. Phys. 12 (2021) 023.
[51] V. Alba and J. Maldacena, Primordial gravity wave background anisotropies, J. High Energy Phys. 03 (2016) 115.
[52] C. R. Contaldi, Anisotropies of gravitational wave backgrounds: A line of sight approach, Phys. Lett. B **771**, 9 (2017).
[53] M. Geller, A. Hook, R. Sundrum, and Y. Tsai, Primordial anisotropies in the gravitational wave background from cosmological phase transitions, Phys. Rev. Lett. **121**, 201303 (2018).
[54] N. Bartolo, D. Bertacca, S. Matarrese, M. Peloso, A. Ricciardone, A. Riotto, and G. Tasinato, Anisotropies and non-gaussianity of the cosmological gravitational wave background, Phys. Rev. D **100**, 121501 (2019).
[55] N. Bartolo, D. Bertacca, V. De Luca, G. Franciolini, S. Matarrese, M. Peloso, A. Ricciardone, A. Riotto, and G. Tasinato, Gravitational wave anisotropies from primordial black holes, J. Cosmol. Astropart. Phys. 02 (2020) 028.
[56] N. Bartolo, D. Bertacca, S. Matarrese, M. Peloso, A. Ricciardone, A. Riotto, and G. Tasinato, Characterizing the cosmological gravitational wave background: Anisotropies and non-Gaussianity, Phys. Rev. D **102**, 023527 (2020).
[57] E. Dimastrogiovanni, M. Fasiello, A. Malhotra, P. D. Meerburg, and G. Orlando, Testing the early universe with anisotropies of the gravitational wave background, J. Cosmol. Astropart. Phys. 02 (2022) 040.
[58] N. Bartolo *et al.* (LISA Cosmology Working Group Collaboration), Probing anisotropies of the stochastic gravitational wave background with LISA, J. Cosmol. Astropart. Phys. 11 (2022) 009.
[59] P. Adshead, N. Afshordi, E. Dimastrogiovanni, M. Fasiello, E. A. Lim, and G. Tasinato, Multimessenger cosmology: Correlating CMB and SGWB measurements, Phys. Rev. D **103**, 023532 (2021).
[60] C. M. F. Mingarelli, T. Sidery, I. Mandel, and A. Vecchio, Characterizing gravitational wave stochastic background anisotropy with pulsar timing arrays, Phys. Rev. D **88**, 062005 (2013).
[61] S. R. Taylor and J. R. Gair, Searching for anisotropic gravitational-wave backgrounds using pulsar timing arrays, Phys. Rev. D **88**, 084001 (2013).
[62] C. M. F. Mingarelli, T. J. W. Lazio, A. Sesana, J. E. Greene, J. A. Ellis, C.-P. Ma, S. Croft, S. Burke-Spolaor, and S. R. Taylor, The local nanohertz gravitational-wave landscape from supermassive black hole binaries, Nat. Astron. **1**, 886 (2017).
[63] S. R. Taylor, R. van Haasteren, and A. Sesana, From bright binaries to bumpy backgrounds: Mapping realistic gravitational wave skies with pulsar-timing arrays, Phys. Rev. D **102**, 084039 (2020).
[64] E. C. Gardiner, L. Z. Kelley, A.-M. Lemke, and A. Mitridate, Beyond the background: Gravitational-wave anisotropy and continuous waves from supermassive black hole binaries, Astrophys. J. **965**, 164 (2024).
[65] G. Sato-Polito and M. Kamionkowski, Exploring the spectrum of stochastic gravitational-wave anisotropies with pulsar timing arrays, Phys. Rev. D **109**, 123544 (2024).
[66] G. Agazie *et al.* (NANOGrav Collaboration), The NANOGrav 15 yr data set: Search for anisotropy in the gravitational-wave background, Astrophys. J. Lett. **956**, L3 (2023).
[67] M. R. Sah, S. Mukherjee, V. Saeedzadeh, A. Babul, M. Tremmel, and T. R. Quinn, Imprints of supermassive black hole evolution on the spectral and spatial anisotropy of nano-hertz stochastic gravitational-wave background, Mon. Not. R. Astron. Soc. **533**, 1568 (2024).
[68] J. Raidal, J. Urrutia, V. Vaskonen, and H. Veermäe, Statistics of the supermassive black hole gravitational wave background anisotropy, arXiv:2411.19692.
[69] G. Cusin and G. Tasinato, Doppler boosting the stochastic gravitational wave background, J. Cosmol. Astropart. Phys. 08 (2022) 036.
[70] D. Chowdhury, G. Tasinato, and I. Zavala, Response of the Einstein telescope to doppler anisotropies, Phys. Rev. D **107**, 083516 (2023).
[71] G. Tasinato, Kinematic anisotropies and pulsar timing arrays, Phys. Rev. D **108**, 103521 (2023).
[72] D. Bertacca, A. Ricciardone, N. Bellomo, A. C. Jenkins, S. Matarrese, A. Raccanelli, T. Regimbau, and M. Sakellariadou, Projection effects on the observed angular spectrum of the astrophysical stochastic gravitational wave background, Phys. Rev. D **101**, 103513 (2020).
[73] L. Valbusa Dall'Armi, A. Ricciardone, and D. Bertacca, The dipole of the astrophysical gravitational-wave background, J. Cosmol. Astropart. Phys. 11 (2022) 040.
[74] A. K.-W. Chung, A. C. Jenkins, J. D. Romano, and M. Sakellariadou, Targeted search for the kinematic dipole of the gravitational-wave background, Phys. Rev. D **106**, 082005 (2022).
[75] G. F. Smoot, M. V. Gorenstein, and R. A. Muller, Detection of anisotropy in the cosmic black body radiation, Phys. Rev. Lett. **39**, 898 (1977).
[76] A. Kogut *et al.*, Dipole anisotropy in the COBE DMR first year sky maps, Astrophys. J. **419**, 1 (1993).
[77] C. L. Bennett *et al.* (WMAP Collaboration), First year Wilkinson Microwave Anisotropy Probe (WMAP) observations: Preliminary maps and basic results, Astrophys. J. Suppl. Ser. **148**, 1 (2003).
[78] N. Aghanim *et al.* (Planck Collaboration), Planck 2013 results. XXVII. Doppler boosting of the CMB: Eppur si muove, Astron. Astrophys. **571**, A27 (2014).
[79] B. Allen and A. C. Ottewill, Detection of anisotropies in the gravitational wave stochastic background, Phys. Rev. D **56**, 545 (1997).
[80] M. Anholm, S. Ballmer, J. D. E. Creighton, L. R. Price, and X. Siemens, Optimal strategies for gravitational wave stochastic background searches in pulsar timing data, Phys. Rev. D **79**, 084030 (2009).
[81] J. Gair, J. D. Romano, S. Taylor, and C. M. F. Mingarelli, Mapping gravitational-wave backgrounds using methods from CMB analysis: Application to pulsar timing arrays, Phys. Rev. D **90**, 082001 (2014).
[82] S. C. Hotinli, M. Kamionkowski, and A. H. Jaffe, The search for anisotropy in the gravitational-wave background with pulsar-timing arrays, Open J. Astrophys. **2**, 8 (2019).
[83] Y. Ali-Haïmoud, T. L. Smith, and C. M. F. Mingarelli, Insights into searches for anisotropies in the nanohertz

gravitational-wave background, Phys. Rev. D **103**, 042009 (2021).
[84] Y. Ali-Haïmoud, T. L. Smith, and C. M. F. Mingarelli, Fisher formalism for anisotropic gravitational-wave background searches with pulsar timing arrays, Phys. Rev. D **102**, 122005 (2020).
[85] P. Auclair *et al.* (LISA Cosmology Working Group), Cosmology with the laser interferometer space antenna, Living Rev. Relativity **26**, 5 (2022).
[86] N. J. Cornish and R. van Haasteren, Mapping the nano-Hertz gravitational wave sky, arXiv:1406.4511.
[87] S. R. Taylor *et al.*, Limits on anisotropy in the nanohertz stochastic gravitational-wave background, Phys. Rev. Lett. **115**, 041101 (2015).
[88] P. F. Depta, V. Domcke, G. Franciolini, and M. Pieroni, Pulsar timing array sensitivity to anisotropies in the gravitational wave background, arXiv:2407.14460.
[89] T. Konstandin, A.-M. Lemke, A. Mitridate, and E. Perboni, The impact of cosmic variance on PTAs anisotropy searches, arXiv:2408.07741.
[90] N. Pol, S. R. Taylor, and J. D. Romano, Forecasting pulsar timing array sensitivity to anisotropy in the stochastic gravitational wave background, Astrophys. J. **940**, 173 (2022).
[91] A.-M. Lemke, A. Mitridate, and K. A. Gersbach, Detecting gravitational wave anisotropies from supermassive black hole binaries, arXiv:2407.08705.
[92] R. C. Bernardo and K.-W. Ng, Charting the nanohertz gravitational wave sky with pulsar timing arrays, arXiv:2409.07955.
[93] M. Maggiore, *Gravitational Waves. Vol. 2: Astrophysics and Cosmology* (Oxford University Press, Oxford, 2018).
[94] M. Maggiore, *Gravitational Waves. Vol. 1: Theory and Experiments* (Oxford University Press, Oxford, 2007).
[95] E. Roebber and G. Holder, Harmonic space analysis of pulsar timing array redshift maps, Astrophys. J. **835**, 21 (2017).
[96] J. Nay, K. K. Boddy, T. L. Smith, and C. M. F. Mingarelli, Harmonic analysis for pulsar timing arrays, Phys. Rev. D **110**, 044062 (2024).
[97] M. Çalışkan, Y. Chen, L. Dai, N. Anil Kumar, I. Stomberg, and X. Xue, Dissecting the stochastic gravitational wave background with astrometry, J. Cosmol. Astropart. Phys. 05 (2024) 030.
[98] F. A. Jenet and J. D. Romano, Understanding the gravitational-wave Hellings and Downs curve for pulsar timing arrays in terms of sound and electromagnetic waves, Am. J. Phys. **83**, 635 (2015).
[99] M. Tegmark, A. Taylor, and A. Heavens, Karhunen-Loeve eigenvalue problems in cosmology: How should we tackle large data sets?, Astrophys. J. **480**, 22 (1997).
[100] G. Agazie *et al.* (NANOGrav Collaboration), The NANOGrav 15 yr data set: Detector characterization and noise budget, Astrophys. J. Lett. **951**, L10 (2023).
[101] E. S. Phinney, A practical theorem on gravitational wave backgrounds, arXiv:astro-ph/0108028.
[102] N. M. J. Cruz, A. Malhotra, G. Tasinato, and I. Zavala, Measuring kinematic anisotropies with pulsar timing arrays, Phys. Rev. D **110**, 063526 (2024).
[103] N. M. J. Cruz, A. Malhotra, G. Tasinato, and I. Zavala, Measuring the circular polarization of gravitational waves with pulsar timing arrays, Phys. Rev. D **110**, 103505 (2024).
[104] A. Heavens, Statistical techniques in cosmology, arXiv:0906.0664.
[105] T.-T. Lu and S.-H. Shiou, Inverses of 2×2 block matrices, Comput. Math. Appl. **43**, 119 (2002).
[106] R. A. Horn and C. R. Johnson, *Matrix Analysis* (Cambridge University Press, Cambridge, England, 2012).
[107] A. Lewis, GetDist: A Python package for analysing Monte Carlo samples, arXiv:1910.13970.
[108] M. Tegmark, How to measure CMB power spectra without losing information, Phys. Rev. D **55**, 5895 (1997).